J Indian Inst Sci, Sept.–Oct 1992, 72, 411–469

IISc THESES ABSTRACTS

Thesis Abstract (Ph.D.)

Numerical simulation of a plane 'canonical' mixing layer using a vortex sheet model

by A. J. Basu.
Research supervisors: R. Narasimha and A. Prabhu.
Department: Aerospace Engineering.

1. Introduction

Since Brown and Roshko's discovery[1] of 'coherent' structures in plane turbulent mixing layer flow, several numerical studies using discrete vortex models have been conducted[2-4]. While such simulations have provided much insight into the nature of the flow, some of the computed results have been quantitatively quite different from relevant experimental data. For instance, the maximum Reynolds stresses computed by Inoue[4] are up to about twice as much, and the maximum third-order moments about eight times as much as the corresponding experimental values. The main difficulty with these simulations is that unduly high fluctuations result if the discrete vortices are points. This difficulty is often overcome by using vortices of finite core, but this procedure introduces an artificial and extraneous parameter whose effect is not precisely known.

2. The model and the numerical scheme used

Since mixing layers studied in laboratory are found to be sensitive to many external parameters[5], any new numerical study should aim to simulate a 'pure' or, as we shall call it, a 'canonical' mixing layer, devoid of the undesirable effects of external parameters, both dynamical and numerical, and thus to gain more definitive understanding of the flow. A canonical mixing layer is defined here as one that is formed downstream of a semiinfinite splitter plate and extends all the way to infinity downstream; this configuration leads to a well-posed problem with answers independent of flow length, which is otherwise a problem because of the long-range vortex interactions[6]. Such a flow, in the limit $Re \to \infty$, may be modelled in terms of the inviscid evolution of an infinitesimally thin vortex sheet shed from the trailing edge of the plate. The boundary layer on the plate is replaced by a vortex sheet that remains bound to the plate at all times; this is achieved by placing on the plate a doublet sheet whose strength distribution is determined by satisfying the boundary condition of zero normal velocity.

To compute the evolution of the vortex sheet over the infinite domain, the following numerical scheme is used. The flow field is divided into four parts: (i) the region upstream of the trailing edge of the splitter plate, (ii) the (main) computational domain, (iii) a variable 'buffer' space, and (iv) the downstream far field (Fig. 1). The upstream region from $x = -\infty$ to $x = x_L$ is replaced by a semiinfinite vortex sheet; since the variation of the u velocity on the plate is found to be negligible, the strength of the sheet may be taken as $\Delta U = U_1 - U_2$ per unit length (U_1 and U_2 are the free-stream velocities above and below the plate). The doublet sheet is found to have a strength that decreases rapidly as one proceeds upstream from the trailing edge, and so can be assumed to extend only up to a finite distance (say from $x = x_{RD}$ to $x = x_{LD}$, Fig. 1).

Inside the computational domain (extending from $x = x_L$ to $x = x_M$), the vortex sheet is divided into short linear elements. At each time-step, the induced velocities at the mid-points of the elements are computed

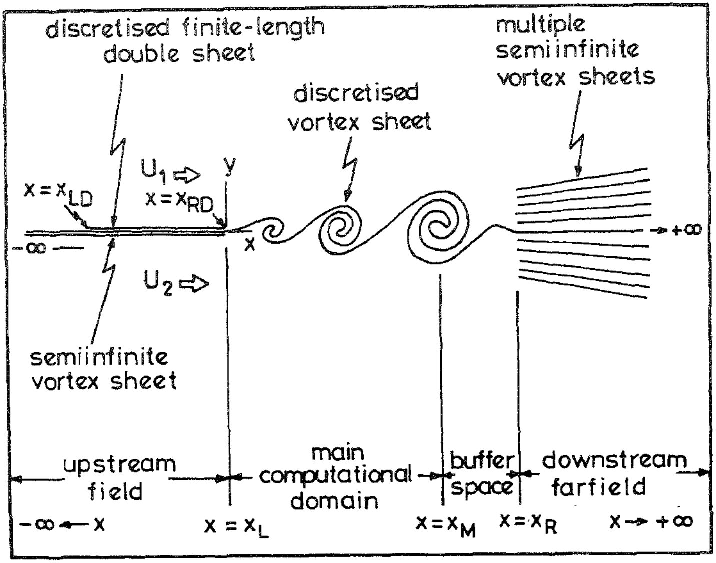

FIG 1. Details of the numerical model.

by direct evaluation of the Biot–Savart integral. The velocities at the end-points (where the integral is singular if neighbouring elements are inclined to each other) are then obtained using a linear interpolation scheme. The elements are moved over each time-step using a first-order Euler time-integration scheme while maintaining the circulation constant. If an element is seen to stretch beyond twice its initial length, it is divided into halves before any further computation is carried on. As each large structure leaves the computational domain, it is accommodated in the 'buffer' space extending from $x = x_M$ to $x = x_R$ (Fig. 1) until the whole structure has left the domain; it is then replaced by the far-field vorticity distribution (discussed later). The buffer space provides a 'soft' coupling between the domain and the downstream far field.

To start with, the downstream far field (from $x = x_R$ to $x = +\infty$) is replaced by a semiinfinite vortex sheet of strength ΔU per unit length. The mean vorticity profile is then computed inside the domain and the downstream far field is replaced by a number of semiinfinite vortex sheets approximating this distribution assuming conical similarity (there is no inherent length scale in this problem). This iterative procedure is repeated until the profile converges in the main domain.

3. Results

The free-stream velocities U_1 and U_2 (normalised by ΔU) are chosen as 2·5 and 1·5, to enable comparison with available experimental[5,7] and numerical[4] data. The computational domain extends from $x_L = 0$ to $X_M = 2$ (initially $x_R = x_M$). The doublet sheet extends from $x_{LD} = -10$ to $x_{RD} = 0$ along the x-axis and

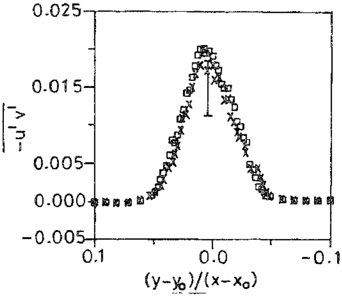

FIG. 2 Computed profile of $-\overline{u'v'}$. x-stations, X. $x = 1{\cdot}5$; □, $x = 1{\cdot}8$ Vertical bar shows the spread of maximum stress values obtained in the laboratory by various investigators.

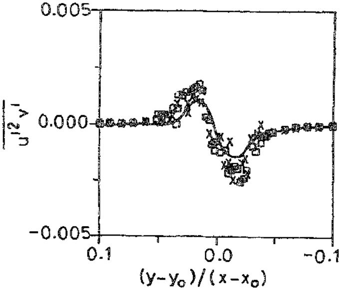

FIG 3 Computed profile of $\overline{u'^2v'}$ x-stations: X, $x = 1{\cdot}5$; □, $x = 1{\cdot}8$. Profile experimentally obtained by Spencer and Jones[7] is shown using solid line for comparison

is divided into 20 constant-strength elements with higher element density near the trailing edge The vortex sheet in the domain is divided initially into 100 constant-strengh elements and is given a small perturbation of wavelength 0·2 and amplitude 0·002 to expedite the rolling up. The time-step is 0·01 time-units.

The calculated mean vorticity profile inside the domain converges after four iterations. A quasi-steady-mixing layer, with linear growth along x, forms inside the domain by time $t = 1$. The mean streamwise velocity profile is found to be within the range of experimental values. The computed mixing layer growth rate $\delta_w' = \delta_w/(x - x_0)$, where $\delta_w = \Delta U/(d\overline{U}/dy)_{\max}$ is the vorticity thickness, and x_0 the x-coordinate of the virtual origin, is about 0·053. This value falls nearly at the centre of the experimental scatter[1] at $\lambda = \Delta U/(U_1 + U_2) = 0{\cdot}25$.

The maxima of the computed profiles of the rms quantities $\hat{u}'$, ($\approx$0·22) and $\hat{v}'$ ($\approx$0·23) are found to be slightly higher than experimental values, which typically range from 0·17 to 0·2 for $\hat{u}'$ and from 0·13 to 0·23 for $\hat{v}'$. The computed profile of the Reynolds shear stress $-\overline{u'v'}$ is shown in Fig. 2 against the non-dimensional parameter $(y - y_0)/(x - x_0)$, where y_0 is the y-coordinate corresponding to local mean velocity $\overline{U} = (U_1 + U_2)/2$. The computed maximum of $-\overline{u'v'}$ is between 0·017 and 0·021 (experimental data range from 0·011 to 0·019).

The profiles of the third-order moments $-\overline{u'^2v'}$ $-\overline{u'v'^2}$, $\overline{u'^3}$ and $\overline{v'^3}$ are averaged over 2200 time-steps. The computed profile of $\overline{u'^2v'}$ is shown in Fig. 3. The computed maximum ($\approx$ 0·0017) and minimum ($\approx$ $-$ 0·0025) of $\overline{u'^2v'}$ are about twice those reported by Spencer and Jones[7] (corresponding values computed by Inoue are 0·006 and $-$0·0053)

The computed changes from the initial values of the total circulation Γ, the first moments of vorticity distribution M_x and M_y, the second moment J, and the Hamiltonian H are found to be small indicating the accuracy of the numerical scheme.

4. Conclusions

The present vortex sheet model of a mixing layer in general gives more realistic values of various flow quantities, in particular the moments of the fluctuating velocities.

References

1. BROWN, G. L. AND ROSHKO, A. *J Fluid Mech*, 1974, **64**, 775–816.

2. Ashurst, W. T. *Turbulent shear flows* (ed., Durst *et al*). Vol 1, 1979, pp 402–413, Springer-Verlag
3. Leonard, A *J. Computational Phys*, 1980, **37**, 289–335
4. Inoue, O. *AIAA J*, 1985, **23**, 367–373
5. Oster, D. and Wygnanski, I. *J Fluid Mech.*, 1982, **123**, 91–130
6. Dimotakis, P E. and Brown, G. L. *J. Fluid Mech*, 1976, **78**, 535–560
7. Spencer, B. W. and Jones, B G. *AIAA Paper*, 1971, 71–613.

Thesis Abstract (Ph.D.)

Investigation of flow over delta wings with leading edge separation by B. M. Hiremath.
Research supervisors: V. S. Holla, S. P. Govinda Raju and A. Prabhu.
Department: Aerospace Engineering.

1. Introduction

Wings of delta planform are well suited for high Mach number flight due to their low wave drag. Further, at low subsonic speeds and at high incidences (corresponding to aircraft taking off and landing) the lifting capacity of these wings is considerably enhanced by the formation of leading edge vortices. Because of these benefits, delta plan form wings are much in use and currently there is large interest in the study of flow past these wings at high incidences.

Flow past delta wings at subsonic speeds has been studied analytically. The first model for such a flow was proposed by Legendre. Later studies based on improved models have been made by Adams[1], Brown and Michael[2], Mangler and Smith[3], Holla and Fernandez[4, 5] and Smith[6]. These studies give detailed information about the strength and position of the leading edge vortex sheet, the vortex core, the spanwise pressure distribution and the normal force.

Experimental studies of delta planform wings are relatively few. One of the earliest such studies was due to Squire[7]. Later studies include those due to Wentz and MacMohan[8] and Earnshaw[9]. More recently, detailed velocity measurements on a series of delta wings including effects of sweepback, angle of attack, spanwise and chordwise camber has been reported by Sforza *et al*[10].

2. Experimental study

There has been an ongoing programme of analytical and experimental research on delta wings in this department. The analytical studies by Fernandez and Holla[5] could locate the position of the leading edge vortex and the position of suction peak on the spanwise cambered thin wings. Static pressure measurements on the wing surface have been reported by Holla and Ramamurthy[11] on wings with spanwise camber. However, detailed flow measurements have not been attempted till now.

In the present investigation, detailed velocity measurements have been made on the wing and in the near wake of a set of three delta wings with a plane, a simple camber and a reflex camber configurations, respectively, all with a span of 80 cm and an aspect ratio of 1·6. They use a thickness distribution of a NACA 16–006 modified section. The wings were tested in 7 × 5′ closed-circuit elliptic test section wind tunnel. Using a blunt conical-nosed five-hole probe, the pressure measurements were made at different chordwise stations on each wing. A 3D probe traverse mechanism was designed and fabricated for making flow field survey measurements at appropriately chosen grid points. The probe was calibrated for yaw and pitch of the approach velocity in a low-speed wind tunnel, which has 20 × 20 × 10″ test section and with a low turbulence level.

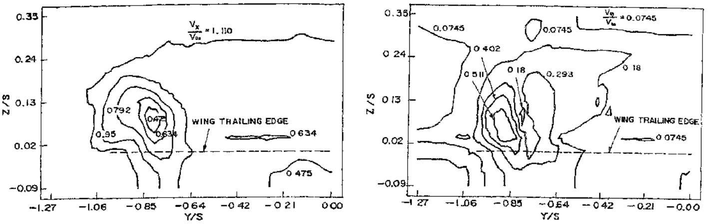

(a) (b)

FIG. 1 Plane wing at $\alpha = 10°$, (a) Axial flow, (b) Cross-flow velocity contour at x/c = 1·18

3. Data analysis

The five-hole probe pressure data were normalised with respect to instantaneous dynamic pressure. Necessary computer programs were developed to obtain the vortex strength and the information at each grid point of the cross-flow plane to plot the following graphs at different chordwise stations of the wings.

1. Total velocity contours.
2. Axial velocity contours.
3. Cross-flow velocity contours.
4. Vorticity contours.
5. Cross-flow velocity vector plots, and
6. Circulation on each half of the wing

Typical plots for a plane wing at $x/c = 1·18$ are given in Figs 1 and 2. Using similar plots for each of the cross-flow planes, the flow characteristics are analysed to obtain information about the vortex core location and the circulation on the port and starboard sides of the wing. The vortex core position is located by using different methods indicated in Table I. Using these data the following studies are made.

1. A study of the behaviour of the leading edge vortices on the wing and in the near wake on all the three wings tested.
2. Comparison of cambered wing characteristics with that of the plane wing.
3. Comparison of the characteristics of the two cambered wings tested.
4. Comparison of these experimental results on the thick wings with theoretical data for thin wings and hence determine the usefulness of the theoretical data on thin wings.
5. Comparison of the results of vortex core location obtained by using different types of plots and find the merits of each method of plotting.

4. Conclusions

1) The present study shows that on the plane wing, at 10° incidence, in respect of vortex strength, symmetry is realised between port and starboard sides. But at 20° incidence a small amount of asymmetry is noticed.

2) For a qualitative assessment of vortex strength and its core location, the total head loss data from the kiel tube would be sufficient

3) As the total velocity contours and the axial velocity contours are similar at all stations, an experiment with a pitot tube would give a fairly good estimate of the vortex strength and its path.

Table I

Vortex core location on port side of thick plane delta wing at 10° incidence

$V = 29{\cdot}9$ to $36{\cdot}89$ m/s Re No = $1{\cdot}99 \times 10^6$ to $2{\cdot}45 \times 10^6$

Chord wise station X/C	Spanwise location y/s							Vertical location z/s by						
	Total velocity contour	Axial velocity contour	Cross-flow velocity contour	Vorticity contour	Cross-velocity vector plot	Kiel tube Expt	Theory (thin wing)	Total velocity contour	Axial velocity contour	Cross-flow velocity contour	Vorticity contour	Cross-velocity vector plot	Kiel tube	Theory (thin wing)
0·3	0·7116	0·7116	0·736	0·822	0·834	–	0·833	0·139	0·139	0·148	0·162	0·1665	–	0·1047
0·4	0·726	0·748	0·814	0·814	0·781	–	0·833	0·120	0·120	0·124	0·169	0·160	–	0·1047
0·5	0·86	0·818	0·765	0·797	0·775	0·81	0·833	0·128	0·120	0·108	0·136	0·132	0·152	0·1047
0·6	0·726	0·814	0·836	0·792	0·836	0·847	0·833	0·128	0·123	0·144	0·124	0·120	0·148	0·1047
0·9	0·892	0·892	0·877	0·979	0·848	0·816	0·833	0·0945	0·0945	0·092	0·095	0·092	0·136	0·1047
1·18	–	0·782	0·859	0·782	0·801	0·842	0·833	–	0·0825	0·066	0·0935	0·0825	0·103	
1·35	–	0·762	0·830	0·762	0·782	–		–	0·115	0·134	0·112	0·115	–	
1·53	–	0·733	0·752	0·733	0·742	–		–	0·866	0·945	0·102	0·0866	–	
1·71	–	0·742	0·821	–	0·752	–		–	0·072	0·051	–	0·072	–	

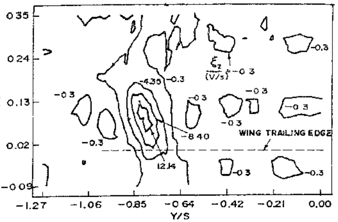

FIG. 2a. Plane wing at α = 10° vorticity contour at x/c = 1·18. ξ = Vorticity, V = Free stream velocity, S = Wing local semispan.

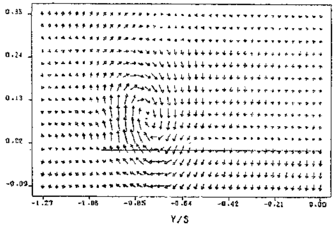

FIG. 2b. Plane wing at α = 10° cross-flow velocity vector plot at x/c = 1·18.

4) At 10° incidence, on the cambered wings, the vortex is weak and grows continuously up to the trailing edge while on the plane wing it is comparatively strong and grows up to x/c = 0·6 on the wing and beyond this station it attenuates gradually. In the wake, on all the three wings, the vortex diffuses as it moves in the streamwise direction. At 20°incidence, on all the three wings the vortex is strong and grows in strength up to x/c = 0·6. Subsequently, on the wing and in the near wake, it attenuates.

5) At 10° incidence, the camber is observed to cause a weakening of the leading edge vortex. But with increase of incidence, the difference in the vortex strength in comparison with that on the plane wing reduces progressively in the middle third region of the wing.

6) At 10° incidence, the vortex core location is more outboard and nearer to the wing surface on the cambered wings as compared to that on the plane wing. This trend is in agreement with theoretical data for thin wings. At 20° incidence, in the spanwise direction, the vortex on the cambered wing lies outboard to that on the plane wing, and in the vertical direction, the vortex on the simple cambered wing is at a greater height above the wing as compared to its position on plane wing. Such a behaviour is consistent with the trend predicted by theory[4, 5].

7) For all the wing configurations and at all stations of measurement, the theoretical estimates of circulation are higher than the measured values.

8) In the wake region, the measured data are insufficient to lead to any firm conclusions.

9) This study shows that the theoretical methods based on the conical flow and slender body theory for thin wings give a fairly good estimate of the vortex core location only in the middle third of the wing chord region.

References

1. ADAMS, M. C. Leading-edge separation from delta wings at supersonic speeds, *J. Aeronaut. Sci.*, 1953, **20**, 430.

2. BROWN, C. E. AND MICHAEL, W. H. JR *On slender delta wings with leading edge separation*, NACA TN 3430, April 1955.

3. MANGLER, K. W. AND SMITH, J. H. B. A theory of flow past a slender delta wing with leading edge seperation, *Proc. R. Soc.* A, 1959, **251**, 200–217; also *RAE Rep. Aero.* 2593, 1957.

4. FERNANDEZ, J. AND HOLLA, V. S. Spanwise cambered delta wings with leading edge separation, *J. Aircr.*, 1977, **14**, 276–282.

5. HOLLA, V. S. AND FERNANDEZ, J. C. Reflex camber delta wings with leading edge separation, *J. Aeronaut. Soc. India*, 1977, **29**, 95–104.

6 Smith, J. H. B. Improved calculations of leading edge separation from slender delta wings, *Proc. R. Soc Lond A*, 1968, **306**, also RAE Technical Report 66070 (1966)

7 Squire, L C *Camber effects on linear lift of slender wings with sharp leading edges*, Aeronautical Research Council, Britain, ARC CP 924, 1967.

8. Wentz, W. H. and MacMohan, M. C. *An experimental investigation flow fields about delta and double delta wings at low speeds*, NASA CR 521, 1966

9. Earnshaw, P. B *An experimental investigation of structure of leading edge vortex*, ARC R&M No 3281, March 1961.

10 Sforza, P. M., Stasi, W., Pazienza, J. and Smorto, M. Flow measurements in leading-edge vortices, *AIAA J.*, 1978, **16**, 218–224

11. Holla, V S. and Ramamurthy, P K. Pressure measurements on two spanwise cambered delta wings with leading edge separation, *J Aeronaut. Soc. India*, 1986, **38**, 21–26.

Thesis Abstract (Ph.D.)

Programmable nonlinear ADCs—Some new techniques by Dinesh K. Anvekar.
Research supervisor: B. S. Sonde.
Department: Electrical Communication Engineering.

1. Introduction

The nonlinear analog to digital converter (NADC) is an important building block in several areas of electronics, *e.g.*, modern instrumentation, digital communication, hybrid computing and signal processing. In these application areas, some of the desirable features for the NADCs are: (i) digital programmability, (ii) IC realizability, (iii) hardware simplicity, and (iv) higher conversion speed

Although several schemes for NADCs have been reported in literature, only a few of them seem to fulfill one or more of the above desirable features. Keeping this in view, it was felt necessary to undertake research work for the development of new NADCs capable of meeting most of the above features together. As a result, several new and interesting NADCs have been developed. The operation of these NADCs has been verified by experimental implementation using state-of-the-art hardware/software, computer simulation, and/or analytical evaluation. The highlights of these NADCs and the results of this research work are given below.

2. Programmable successive approximation NADCs

In this class of NADCs, the main emphasis has been on achieving digital programmability by using optimal-sized ROM, or PLS in the successive approximation loop while at the same time optimizing the conversion speed. The highlights of these NADCs are as follows:

2.1. *NADC using optimal-sized ROM*

In this NADC, optimal-sized ROM is used in place of SAR. A new technique of using LSB of the ROM address to hold the comparator output is utilized to minimize the ROM size. As compared to a reported NADC, considerable reduction in ROM size is possible here, *e.g.*, 96 per cent for PCM codec application. This leads to appreciable reduction in the die area required for the fabrication of NADC in IC form.

2.2. *ROM-prefetch high-speed NADC*

While the above NADC has optimal-sized ROM, its speed is limited by the ROM access time, which is generally large. This problem is overcome here by separating the ROM from the successive approximation loop, and by using a shift register instead of an SAR in the NADC realization. This leads to a net lower conversion time for the NADC due to the prefetching of successive approximation codes from the ROM during the time the DAC-comparator loop is settling. The ROM requirement for this NADC is still the minimum required for obtaining an arbitrary nonlinear characteristic, making IC realization in this case also economical.

2.3. *High-speed hybrid NADC*

In this NADC, a much higher conversion speed is achieved by combining the techniques of flash ADC and successive approximation ADC. In general, if a p-bit flash ADC is used, then an pn-bit conversion is completed in only n cycles In practice, as larger values of p lead to higher hardware complexity, $p = 2$ or 3 is economically justified. Thus, with $p = 2$, a $2n$-bit conversion can be completed in only n clock cycles. This speed up in conversion is achieved at the cost of two additional DACs and comparators, and nominally extra ROM size, making this NADC suitable for high-speed real-time applications.

2.4. *Piecewise linear approximation NADC*

This NADC can be digitally programmed by knowing only the end-points of the segments in the piecewise linear approximation of the nonlinear characteristic. An important feature of this new NADC is the programmability even for nonlinear characteristics approximated by linear segments with unequal digital intervals. Thus, this NADC is superior to the piecewise linear approximation NADC reported in literature.

2.5. *PLS-based NADC*

In this NADC, digital programmability is achieved by using a PLS instead of ROM. As the PLS delay is usually much smaller than the ROM access time, a much higher conversion speed is possible with this NADC, as compared to a similar NADC using ROM. The CAD algorithm developed for the logic simplification in this case can be incorporated in the CAD software for automated programming of the PLS This indeed helps in reducing the turn-around time for the design of such NADCs.

3. Switched-capacitor NADCs

This family of NADCs is particularly important in MOS/CMOS IC form, because the A/D conversion is performed by the manipulation of the charge stored in the MOS capacitors which are interconnected by analog switches. Here, digital programmability is achieved by controlling the switching sequence of the analog switches. The highlights of these NADCs are as follows:

3.1. *Curve-runup and curve-rundown NADCs*

A new technique of stepped nonlinear curve generation using a switched-capacitor integrator is used in these NADCs. As the slope of the nonlinear curve at any point is controlled by the ROM output, the transfer characteristic realized by these NADCs is easily programmable by changing the ROM contents. Simplicity of the circuit blocks enables economical monolithic IC implementation of both these NADCs, whereas their digital programmability makes them useful for interfacing nonlinear transducers to programmable instrumentation systems.

3.2. *Charge-balancing NADC*

This NADC is an extension of a reported charge-balancing ADC to the nonlinear case by the addition of ROM and extra hardware in the digital logic section. The transfer characteristic of the NADC is easily programmable by changing the contents of the ROM. The use of standard building blocks in the digital section, the parasitic- and gain-insensitive configuration of the switched-capacitor circuit, and the capacitance ratio independence of the conversion process make this NADC easily realizable in IC form.

3.3. *Improved A-law-encoding NADC*

In this NADC, A-law PCM encoding is achieved by successive approximation steps consisting of charge redistribution in a binary weighted capacitor array. The chip area required for the capacitors of this NADC is about 65–75 per cent less as compared to some of the reported designs. Thus, the incorporation of this NADC in codecs can considerably minimize the overall IC cost.

3.4 *Algorithmic A-law NADC*

In this NADC, the A-law PCM word is obtained by the logical interpretation of the bits resulting from algorithmic A/D conversion of the input voltage. As only a few ratio-independent capacitors are required for this A/D conversion, very economical implementation of the NADC in a small chip area is possible. The operation can also be extended to u-law PCM encoding.

4. Multimicroprocessor-based NADC system[1]

This NADC system is useful for higher speed processing for the elimination of errors due to nonlinearity and disturbing variables on transducer output signal as also for other high-speed real-time instrumentation applications. The noteworthy features of the architecture of the multimicroprocessor system are:

(i) Use of dual-port RAMs for conflict-free interprocessor data transfers;

(ii) A new concept of blackboard memory for high-speed common-data transfer among the microprocessors.

The important results of performance evaluation of the NADC system with typical task allocation for the microprocessors are:

(i) Significant improvement in processing speed by the use of dual- or triple-microprocessor systems as compared to a single microprocessor system;

(ii) Superiority of the dual-microprocessor system over the triple microprocessor system with regard to cost-effectiveness;

(iii) Possibility of higher processing speed by using more than three microprocessors, but with much lower cost-effectiveness.

Reference

1. Anvekar, D. K. and Sonde, B. S.	Transducer output signal processing using dual and triple microprocessor systems, *IEEE Trans.*, 1989, **IM-38**, 834–836.

Thesis Abstract (Ph.D.)

Studies on the degradation of tin oxide/silicon interfaces by Uma Raychaudhuri.
Research supervisors: M. Satyam, K. Ramkumar and D. B. Ghare.
Department: Electrical Communication Engineering.

1. Introduction

In the last few years, tin oxide (SnO_2)/n silicon solar cells have been proposed by some as low-cost photovoltaic devices. The photovoltaic properties of SnO_2/n Si heterojunctions prepared by spray pyrolysis have been studied by several investigators[1,2]. However, basic mechanisms, such as carrier transport across the hetero-junction, dependence of device characteristics as well as the degradation of these characteristics with ageing on interface parameters such as traps are yet to be understood. In this work, an attempt has been made to find out the various reasons that may be responsible for the observed degradation of the SnO_2/n Si cells.

2. Experimental details

The experiments consist of two parts: (i) preparation (by spray pyrolysis)[3] and characterization of tin oxide films before and after ageing, (ii) preparation and characterization of SnO_2/n Si interfaces[4] before and after ageing.

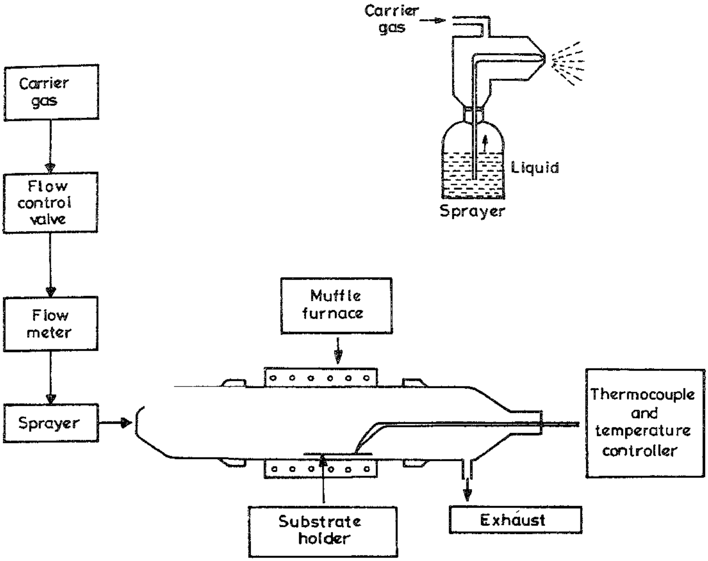

FIG. 1. Crosssectional view of tin oxide film spraying set-up.

Figure 1 shows the spray setup used in this investigation. The structural, electrical and optical properties of the SnO_2 films have been studied as the substrate temperature and deposition times are changed while keeping other parameters constant at standard values as reported by previous investigators. These properties are again measured after ageing for one year.

SnO_2/n Si interfaces have been fabricated by depositing SnO_2 films on Si substrates by spray pyrolysis. Three types of samples have been prepared.

a) Samples in which SnO_2 has been directly deposited on Si (n-type) substrates (named as INI-X),

b) Samples in which a thin SiO_2 layer is interposed between SnO_2 and Si (named as OX-Y); and

c) INI-X samples which are heated in oxygen atmosphere (named as OXAN-2).

These samples have been characterized by the measurement of I–V and photo-voltaic characteristics before and after ageing.

3. Results and discussion

3.1. *Studies on SnO_2 film*

1. X-ray and ESCA indicate that SnO_2 film is formed by the above process.

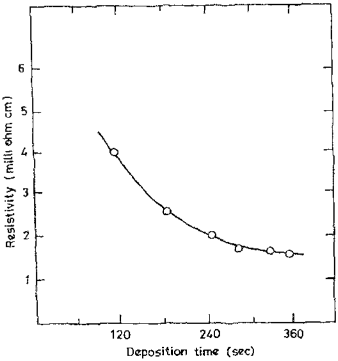

FIG 2. Variation of resistivity with deposition time for SnO_2 films at substrate temperature of 360°C.

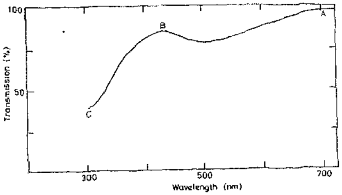

FIG 3. Optical transmission characteristics of a typical SnO_2 film.

2. Resistivity of the film decreases with film thickness (*i.e.*, deposition time (Fig. 2)). This variation can be explained by solving an appropriate diffusion equation of alcohol vapours which reduce SnO_2 film leading to oxygen vacancies which impart electrical conductivity.
3. Optical transmission spectrum of the film shows gradual absorption edge (Fig. 3). This can be explained by a model which assumes uniformly distributed defect energy levels in the bandgap and the resulting transitions of electrons among these levels due to the incident radiation.

With ageing the absorption edge shifts to higher energy. This is possible if oxygen diffuses through SnO_2 film and reduces oxygen defects. This speculation is supported by the observed increase in resistivity of film after ageing.

3.2. *Studies on SnO_2/n Si interface*

1. Ln I *vs* curves of INI-X samples exhibited two linear regions (Fig. 4). It has been found that the observed dependence of such curves on Si resistivity and temperatures could not be explained by any single known theory of carrier transport. A new model has been proposed. It has been proposed that there are two simultaneous current transport processes at the interface. One is trap-assisted current where valence electrons from Si enter the trap levels lying in the energy gap of SnO_2 because there are some traps which are available at nearly the same energy levels (Fig. 5). The electrons from these energy levels are then emitted to conduction band of SnO_2. The second component of current is due to the electron in the conduction band of Si crossing the barrier at the interface by thermoionic emission and/or by diffusion. Based on this model, the observed I–V curves and also their dependence on Si resistivity and temperature have been explained.

At equilibrium the rate of filling of the traps at the interface is equal to the rate of release from them.

Therefore,

$$K_I(N_t - N_{tf})dV = K_2[\exp - (E_c - E_t - V)/KT]N_{tf}\, dV$$

where N_t is the number of available traps at interface, N_{ft} the number of filled traps, and K_1, K_2 are constants.

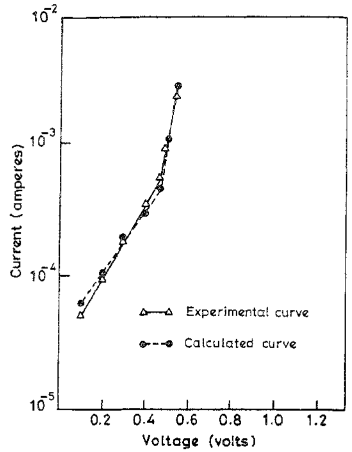

FIG. 4. I-V characteristics of a typical SnO_2/n-Si cell in forward direction.

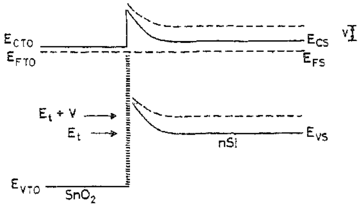

FIG. 5 Energy-band diagram of SnO_2/n-Si.

$$N_{tf} = \frac{K_1 N_t}{K_1 + K_2 \exp \ -(E_c - E_t - V)/KT} \cdot$$

Therefore, the rate of emission of carriers from the traps located between E_t and $E_t + V$ is

$$\int_{E_t}^{E_t + V} K_2 N_{tf} \exp \frac{-\ (E_c - E_t - V)}{KT} \, dV.$$

The trap-assisted current is proportional to this emission rate. After simplification the current becomes,

$$I = I_{01} \, [e^{\frac{qV'}{nKT}} - 1]$$

where $$I_{01} = \text{const. } N_t \cdot N_2 \exp \frac{-\ E + 2E_t}{KT} \cdot KT.$$

It can be shown that $n > 1$.

2. LnI *vs* V curves for OX-y samples exhibited ore linear region. It is speculated that the traps at the interface are passivated by the thin SiO_2 layer and therefore the trap-assisted component and current are not detectable.

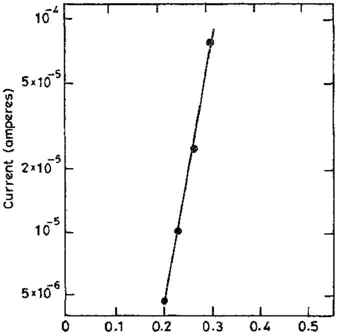

FIG 6. I-V characteristics of a typical SnO_2/SiO_2/n-Si cell in forward direction.

3. LnI *vs* V curves after ageing of the samples for one year indicated that current increased in OX-y samples while in the INI-X samples it showed a decrease. With ageing oxygen diffuses through SnO_2 to the interface and passivates some traps and hence the decrease in current with ageing in INI-X samples. For OX-y samples the trap-assisted current is negligible and with ageing the reduction of traps leads to reduction in barrier height and hence the increase in the observed current.
4. OXAN-Z samples exhibit similar behaviour as that of aged samples implying that on ageing the defect states are reduced in the energy gap due to oxidation[4].

The variation ov V_{oc} for all the groups of samples has been found to be compatible with variations in dark current.

3. Conclusion

Based on the above results it is concluded that the slow penetration of oxygen with time into SnO_2 film and to the interfact is responsible for the degradation of SnO_2/n Si interface which perhaps are responsible for the degradation of SnO_2/Si solar cells

References

1. BUBE, R H., BUCH, F., FAHRENBRUCH, A L , MA, Y Y. AND MITCHELL, K W. Photovoltaic energy conversion with n-CdS-p-CdTe heterojunctions and other II-VI junctions, *IEEE Trans.*, 1977, **ED-24**, 487–492
2. SZCZYRBOWSKI, J., DIETRICH, A. AND HOFFMAN, H. Optical and electrical properties of RF-sputtered indium-tin oxide films, *Phys. Stat Sol* A, 1983, **78**, 243–252
3. VERMA, S., RAO, K. V. AND KAR, S Electrical characteristics of silicon-tin oxide heterojunction prepared by chemical vapour deposition, *J Appl. Phys.*, 1984, **56**, 2812–2822.
4. SHANTHI, E., DUTTA, V., BANERJEE, A. AND CHOPRA, K L Electrical and optical properties of undoped and antimony doped tin oxide films, *J. Appl. Phys.*, 1980, **51**, 6243–6251.

Thesis Abstract (Ph.D.)

Digital models for analysis and synthesis of ECG by M. Ramasubba Reddy.
Research supervisor: I. S. N. Murthy.
Department: Electrical Engineering.

1. Introduction

The study of cardiac electrical activity — its origin and propagation through various pathways and muscle tissues — in health and disease is the science of electrocardiography. ECG analysis has a long history of four decades outside the domain of the clinician and is one of the extensively studied physiological signals in the present-day clinical medicine for the diagnosis of cardiac disorders. Delineation of the component waves P, QRS, and T present in a given beat is fundamental to the methods of ECG — morphological study, rhythm analysis, data reduction. ECG analysis methods reported in literature till date can be classified as time- and frequency-domain analysis, or a combination of both, syntactic pattern recognition, heuristic and knowledge-based expert system and dipole field theory approaches, and pole–zero modelling, etc. Fairly well-defined characteristics with high slopes and amplitude will facilitate reliable detection of QRS complex in ECG waveform. The small amplitudes with similar slopes compared to those of QRS complex make the recognition of P and T waves difficult. There are not many methods in literature for detection and delineation of P and T waves, though these waves play greater role in the identification of some abnormalities like premature ventricular contractions (PVCs), inverted T waves in the case of MI patients, etc[1].

The work provides the necessary thrust for a complete and total solution of this fundamental problem. The mathematical aspects of the forward and inverse transforms of discrete cosine transform (DCT), discrete sine transform (DST) with their linearity property[2], the modelling techniques of Steiglitz–McBridge and Shanks and the design aspect of FIR filters[3] are briefly presented for ready reference.

2. Method

A parametric model is proposed that fits in a general framework in that the component waves of the signal are treated as events independent of each other and follows signal genesis aspects in a natural way. The model is conceived as consisting of three (or more) subsystems in parallel to account for all the three (or more) component waves. Since it is not possible to model the direct time-domain signal, discrete cosine transformed (DCT) version of the signal is used. The output, the impulse response of each subsystem when inverse transformed (IDCT), gives a component wave and the ECG signal is derived as the output from the whole system. The method uses minimum number of parameters in its model while preserving high accuracy of signal approximation and is a fruitful proposition for efficient signal representation. The method establishes for the first time a direct relationship between the model parameters and waveform features, *i.e.*, between system poles and zeros and the P, QRS, and T component waves of the time signal. A combination of the discrete cosine transform (DCT), a member from the family of orthogonal transformations and the Steiglitz–McBride method, a recursive algorithm is used for estimating the model parameters of a stable signal. The model comprises a system function driven by an impulse source for efficient representation of the ECG signal. A bell-shaped biphasic wave required two poles and two zeros in its system function while a triphasic wave needed an order (4, 4), that is, it is shown that DCTs of bi- and triphasic waves are the same as the impulse response of second- and fourth-order systems, respectively. The upright and inverted bells have identical representations for their transforms as well as system functions but for a change of sign. The ECG signal considered to be made up of such bell-shaped component waves allows to determine model order in a simple way. A study of spectrum of the transformed signal confirmed these model orders. While a normal wave with biphasic P, QRS and T waves required an order (6, 6), abnormal beats of bizarre type required higher orders (10, 10) or (12, 12) in their models. The results show that bizarre waves require higher orders than normals and a zero outside the unit circle for an inverted component wave. The pole-zero model obtained is then utilized propitiously for signal analysis and synthesis, *i.e.*, not only for identification and delineation of the component waves but also for the synthesis of different waveforms. To study the effect of transforms on signal representation, time-domain signal is transformed using DST instead of DCT. The results showed that DCT version of signal can be modelled better. When DCT and DST transformed signals are modelled using Steiglitz–McBride and Shanks methods, it is observed that the Steiglitz–McBride method gave superior results compared to Shanks method. To check the system order selection for a given signal a transformed normal ECG beat is modelled with systems of order (2, 2), (4, 4), (6, 6) and (8, 8). The model output gave only QRS complex when system order is (2, 2), QRS complex and T wave when it is (4, 4), and all the three components P, QRS and T, when the system order is increased to (6, 6). Further increase in system order reduced the normalized mean square error in the model output. These results confirmed the proposition that each biphasic component requires an order of (2, 2) and also shows that larger time domain peaks will get modelled in that order. In this simple way any time-domain signal of m peaks can be modelled with system order ($2m$, $2m$). The results are evaluated in both qualitative and quantitative terms. The model performance is found to be highly satisfactory. While a comparison of model output with the original signal gave an excellent visual match, and the normalized mean square error between the two is well within a reasonable limit of 5 to 10 per cent, best results are obtained when the number of zeros is equal to the number of poles in the model and the algorithm converged in three to five iterations in most of the cases. The deletion of one (or more) pole(s) at a time, from the pole-zero plot, has resulted in the suppression of one (or more) component wave(s) in the model output. Thus, this study not only establishes a one-to-one correspondence between the model pole(s) and the component wave(s) in the time signal but also a way of component delineation from a given signal. The synthesis of desired waveform is attempted by modifying/altering the pole-zero plot of a normal waveform. Using background knowledge on modelling, various abnormal waveforms such as ST elevation, R on T, PVC, etc., have been synthesised.

The transformed signal specturm showed distinct peaks and valleys corresponding to each component wave in contrast to the featureless counterpart computed from the direct time signal. This aspect is exploited to determine the characteristics of suitable filters which are in turn used to filter the transformed signal. The filter output when inverse transformed gives the required component wave. The method is found to give fairly accurate and unambiguous delineation of a given signal into its component waves. The method is then extended to signals containing more than one beat in a single frame. All these aspects are illustrated with extensive examples.

Finally, real-time implementation details of a nonlinear transformation for the delineation of P, QRS, and T waves and determination of their durations from a given ECG waveform are given. The transformation which is in the form of a set of recursive relations has been implemented on Intel 8086 microprocessor-based system. Data acquisition module, numeric data processor and other modules along with the system have been developed to enable the implementation of the algorithm in real time.

3. Results and conclusions

A digital model for the generation of ECG signal is developed from a system theoretic point of view. This pole-zero model approximated both normal and abnormal beats with high accuracy and with minimum number of parameters and more importantly established a direct relationship between the model parameters and P, QRS, T component waves of the signal This naturally leads to the delineation of a given ECG signal into its component waves as well as synthesis of abnormal waveforms of different types by modifying the pole-zero pattern of a normal signal. Development of a more formal method of filtering the transformed signal enabled unambiguous and very accurate delineation of the component waves in a given signal. The component waves of a given ECG signal are delineated in real time using the direct time-domain signal through the execution of a nonlinear transform on a microprocessor system developed specially for the purpose using 8086 processor and a numeric coprocessor.

4. Scope for further work

The techniques presented for both modelling the ECG signal and delineating the component waves by linear filtering a given signal hold great promise and are expected to lead to new directions in the analysis of other biosignals such as respiratory signals, blood pressure waveforms, and signals containing waveforms similar to rectangular, triangular and the like and arbitrary waveforms with well-defined peaks in other fields such as seismology, speech, etc.

References

1. Pahlm, O and Sornmo, L — Software QRS detection in ambulatory monitoring-a review, *Med Biol. Engng*, 1984, 23, 289–297
2. Elliott, D F — *Handbook of digital signal processing Engineering applications*, 1987, Academic Press
3. Box, G E. P. and Jenkins, G M — *Time series analysis–Forecasting and control*, 1976, Holden Day, San Francisco.
4. Durga Prasad, G. S S — *A comparative study of suboptimal ARMA algorithms for biomedical signals*, Ph D Thesis, Department of Electrical Engineering, Indian Institute of Science, Bangalore, India, 1988.

Thesis Abstract (Ph.D.)

Some contributions to the instrumentation techniques for ultrasonic measurements by Laxman Pathak.

Research supervisors: E. S. Raja Gopal and V. S. Raghunathan.

Department: Instrumentation and Services Unit.

1. Introduction

Ultrasonics has a wide range of scientific and engineering applications. The scientific applications include study of material properties, while the engineering applications include nondestructive testing, flow and thickness measurement, leak detection, etc. The instrumentation for scientific applications requires high resolution. Engineering applications, on the other hand, require instruments capable of working reliably in hostile environments.

In the present work the use of ultrasonic techniques to two specialised applications is described. The first is the development / improvement of the instrumentation used for high-resolution ultrasonic measurements which includes the development of automatic echo-select logic for attenuation measurement, and stand-alone pulse-echo-overlap facility for velocity measurement. The second is the development of an instrument using pulse-echo principle, code named BAT, for profiling dimensional deviations of in-reactor components of the fast-breeder test reactor at Kalpakkam.

2. Automatic echo-select logic for attenuation measurement

Ultrasonic attenuation coefficient is measured by introducing a burst of ultrasonic energy in the sample and finding the ratio of the amplitudes of two selected echoes. The amplitude of the echoes in general is related by

$$A_2 = A_1\, e^{-\alpha d}$$

where A_1 and A_2 are the amplitudes of the two echoes and d is the distance travelled between registering the two echoes and α the attenuation coefficient[1].

It can be clearly seen that the measurement of the attenuation coefficient depends upon the precise location and measurement of the echo peaks. When the attenuation is measured as a function of some varying parameter such as temperature, the transit time through the sample also varies resulting in the shift of the echo position. This calls for the adjustment of the sample and hold circuits[2]. A novel automatic echo-select logic was developed for attenuation measurement which eliminates manual intervention during the experiment, thereby improving the accuracy of measurement. The echo-select logic developed latches on to the selected echoes to eliminate this manual adjustment. Figure 1 shows the block diagram of automatic echo-select logic. The echo train received by the transducer is amplified and the envelop of the echo train is fed as input to the echo-select logic. This in turn generates discharge pulses to abort the two

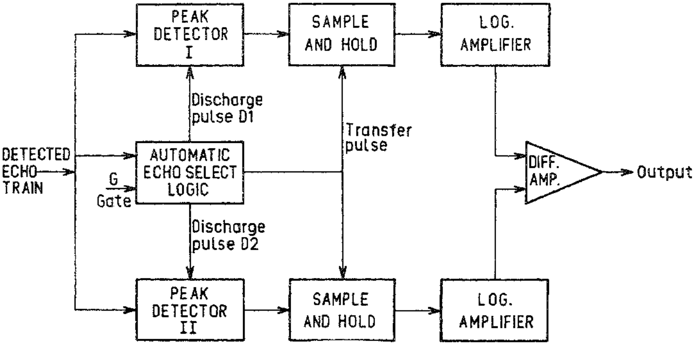

FIG. 1 Block diagram of automatic echo selection scheme

peak detectors until the selected echoes arrive. The selected pulses are then stored on sample holds. The logarithmic difference of the held peaks give the value of the attenuation coefficient. Since the selection and detection of the peaks are done automatically, the measured value is always a true representation of the attenuation coefficient, and is free from the problems due to peak drifts. The logic is implemented using easily available TTL counters and comparators. Attenuation measurement between any two echoes can be easily made by the selection of echo numbers by means of thumbwheel switches[3, 4]. This logic makes the attenuation measurement amenable to microprocessor control.

3. Stand-alone pulse-echo-overlap facility for velocity measurement

For ultrasonic velocity measurement, the time difference between any two echoes is measured. Of various techniques available for velocity measurement, the pulse-echo-overlap technique is very popular since it permits simultaneous measurement of attenuation and velocity and requires only two good echoes for a measurement[5]. A stand-alone unit for velocity measurement has been developed based on pulse-echo-overlap technique.

The circuit diagram of a stand-alone pulse-echo-overlap system is shown in Fig. 2. Since the resolution of frequency synthesizer decides the resolution of velocity measurement, a digital frequency synthesizer of 0·01 Hz resolution in 1 MHz was designed and developed but is described elsewhere[6]. A broadband pulse of 230 V amplitude, generated using P 203 IC, excites the transducer bonded closely to the specimen. The received echoes are fed to the Y-input of an oscilloscope. By careful adjustment of the trigger rate of the oscilloscope (the X-input), it is possible to see two echoes of the echo train overlapped on the screen Under this condition of overlap, the trigger rate applied to the input of the oscilloscope gives the travel time and thus the velocity of sound in the specimen. To aid the overlap, a decade fraction of the trigger pulses fed at X-input is used to trigger the high-voltage pulse generator P203. Additional intensifying pulses are generated using adjustable delays to intensify the beam at selected echoes. Overlap technique requires in general oscilloscope with intensity modulation facility to intensify the selected echoes. An alternative strategy was adopted wherein intensifying pulses and received echo train are added in operational amplifier thereby driving the oscilloscope beam out of screen when selected echoes are not present. This enables one to use ordinary oscilloscope without intensity modulation facility[7].

The stand-alone pulse-echo-overlap system was employed in the residual stress evaluation in stainless steel specimens. The velocity of ultrasonic waves in a material depends upon the elastic properties of the

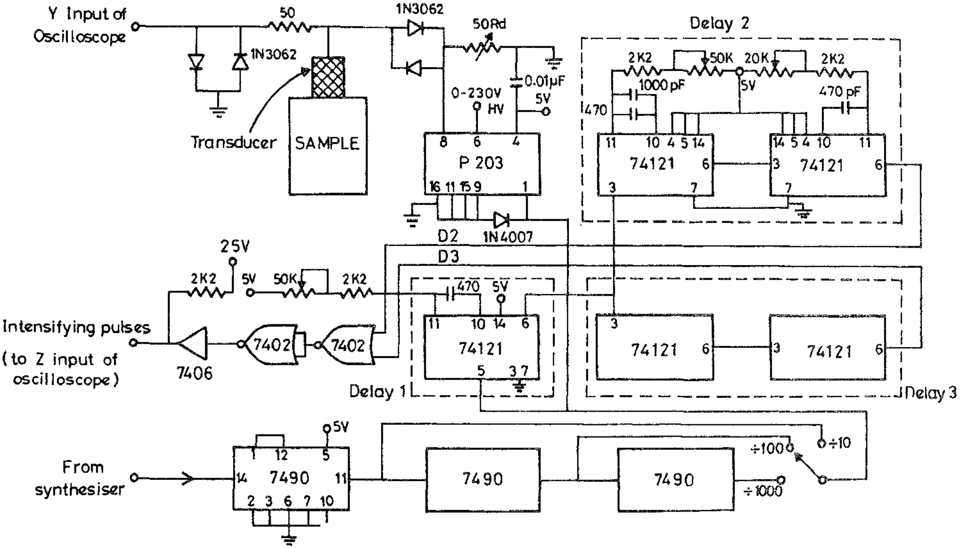

FIG. 2. Circuit diagram of stand-alone pulse-echo-overlap system.

medium. Therefore, when a material deforms in response to an applied load, a small shift in ultrasonic velocity occurs. The velocity and the stress in the material are related by the following equation:

$$V = V_o + A\sigma$$

where V is the actual measured velocity, V_o the velocity of ultrasound in the material free from stress, A the acoustoelastic constant and σ the residual stress. Thus, by measuring velocity on a reference, stress-free specimen and then evaluating the velocity in the material under investigation, the residual stress can be found[8].

4. Profiling of guide tube

During a fuel-handling operation, a large component (guide tube) inside the primary reactor vessel of the FBTR (fast-breeder test reactor) developed an unexpected bend[9–10]. Further operation of the reactor was impossible without replacing the defective component with a new one. Efforts to retrieve the bent tube by pulling were futile, indicating a large bend. Lifting the reactor plug, in which guide tube was mounted and removing the guide tube was a major operation requiring a year's time. An alternative solution was to cut the defective tube inside into two segments which could be retrieved. It was necessary to profile the guide tube to see if it could be removed after cutting into two pieces. Various methods were conceived and some were attempted, with different degree of success. Of these, ultrasonic method, described here, was capable of profiling the entire 3-m length of the guide tube, even in the presence of multiple bends.

While designing the system, it had to be borne in mind that measurement had to be done in reactor with associated problems of limited accessibility for profiling device, and high ambient temperature of about 180°C. For this purpose, an ultrasonic probe for profile measurement using air transducers of 40 KHz frequency was developed, based on a pulse-echo-ranging technique. Profile generated using this method did not require any extrapolations and the measured deviations could be trusted to within 20 mm.

Though pulse-echo-ranging technique is commonly used in radar, ultrasonic level meter and other applications, the challenges involved in the adoption of this technique for the guide tube profiling were: (i) Experiments had to be done in a hostile environment; (ii) The problem due to beam divergence (at 40 KHz it is considerable) had to be tackled; (iii) Commercially available transducers had to be modified to withstand the temperatures of about 180°C; (iv) Provision for cooling the detector assembly had to be made; (v) Correct for velocity coefficient of sound in argon medium at varying temperatures, since the temperature profile inside the reactor was not known; (vi) Correct values of deflection of guide tube at each elevation even in the presence of multiple bends in different planes; (vii) Capture the ultrasonic echo waveforms and store them in a computer for further analysis, since multiple runs of profiling in a sodium-drained condition of the FBTR were not possible.

The divergence problem was overcome by designing suitable acoustic waveguides into the mechanical assembly. The mechanical assembly itself was designed to provide for external injection of argon to cool the transducers. The transducers produced from the market were dismounted and were reassembled using high-temperature-resistant adhesives and were tested in mock-up environments. After several trials, transducers working up to 180°C with cooling arrangements were made.

Suitable software was developed on an IBM PC/XT which was connected to the instrumentation to calculate the deflection in the presence of multiple bends. A fast data acquisition system was designed to capture the echo waveforms and store them in memory of the PC/XT for further analysis.

After several mock-up trials the guide tube was profiled *in situ*. Figure 3 shows *in situ* profiling. From the profile thus obtained, it was possible to confirm that the cut pieces of guide tube could be removed without any problem. It was found later from the cut segments of the guide tube that the profile and deflection deduced from the ultrasonic measurements were in close agreement with the actual shape of the bent guide tube.

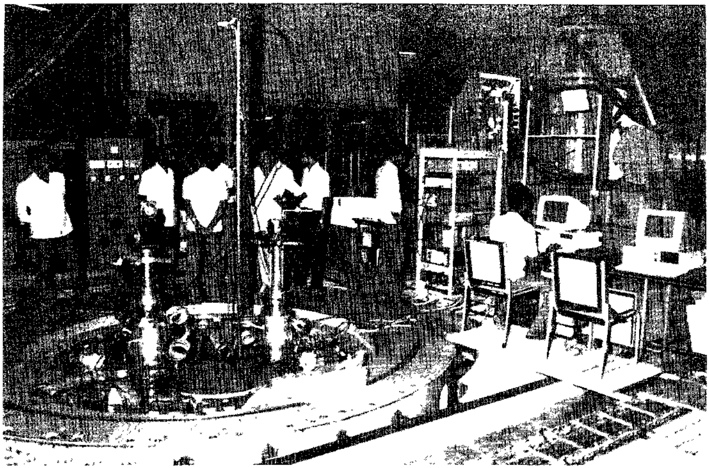

FIG. 3 *In situ* guide tube profiling.

5. Conclusions

Application of ultrasonic techniques in scientific and a specific engineering problem have been discussed. Methods of improving the measurement accuracy of ultrasonic attenuation in laboratory environment, using the novel automatic echo-select logic has been dealt with. The pulse-echo overlap method of measuring the ultrasonic velocity has advantages over other methods. Simple circuit innovations to make this measurement easy using ordinary oscilloscope and a broadband excitation source are described. A stand-alone equipment using the above circuit has been used to find the residual stress in stainless steel samples with good accuracy.

The technique of pulse-echo ranging has been applied to a practical problem of profiling an inaccessible reactor component has been discussed. Various design features to overcome the field-related difficulties in adapting the technique to achieve an accurate solution have been brought out Ultrasonics, in combination with the capabilities of computers, has great potential of becoming a powerful analysis and engineering tool of the future

References

1 TRUELL, R , ELBAUM, C AND CHICK, B.	*Ultrasonic methods in solid-state physics,* 1969, Academic Press
2 HELLIER, A G , PALMER, S B AND WHITEHEAD, D G	An integrated circuit pulse echo overlap facility for measurement of velocity of sound, *J Phys. E,* 1975, **8**, 352–353
3 PATHAK, L , MURALI, N , AND USHA RANI, S.	Automatic echo selection logic for ultrasonic attenuation measurement system, *Rev. Sci Instrum.*, 1983, **54**, 482–485.

4. Pathak, L and Seshadri, V R — Modified automatic echo selection logic for ultrasonic attenuation measurement system, *Rev Sci Instrum.*, 1984, **55**, 1168–1169

5 Papadakis, E P — *Physical acoustics*, Vol. 12 (eds, W P Mason and R N Thurston), 1976, Academic Press.

6 Pathak, L., Murali, N. and Amritha, V P. — Stand-alone pulse-echo-overlap facility for ultrasonic wave transit time measurements. *Rev Sci Instrum*, 1984, **55**, 1817–1822

7 Pathak, L and Palanisami, K — Achieving pulse-echo overlap with scopes having no intensity modulation, *Rev Sci Instrum*, 1986, **57**, 123–124

8 Palanichamy, P, Subramaniam, C V. and Baldev Raj — Couplant correction for ultrasonic measurement, *Br J NDT*, 1989, **31**, 78–81

9 — *Proc. Int Symp. on Fast Breeder Reactor as a Future Source of Power*, Kalpakkam, India, 16–17 December, 1985

10 Evans, P V. — Fast breeder reactors, *Proc Conf. Fast Breeder Reactors*, London, May 17–19, 1966

Thesis Abstract (Ph.D.)

Thermodynamic studies on selected ceramic oxide systems by G. M. Kale.
Research supervisors: K. T. Jacob and G. N. K. Iyengar.
Department: Metallurgy.

1. Introduction

The ever-increasing demand for new materials with improved physical, chemical and mechanical properties for applications in high-technology areas at elevated temperatures has stimulated interest in systematic investigation of phase relations in multicomponent ceramic oxide systems and thermodynamic properties of several ternary oxides. These data are useful for assessing materials compatibility in a number of applications. Accurate thermodynamic data on interoxide compounds are essential for computer generation of reliable phase diagrams. Hence, focus of the investigations is on determination of correct phase relations and accurate thermodynamic data in selected technologically important ceramic oxide systems in which the data are either not available or are inconsistent.

2. Experimental methods

In the study of several ceramic oxide systems, phase relations were obtained by phase characterization after isothermal equilibrium of the mixtures of known initial composition. The equilibrium phase mixtures were characterized by optical microscopy, x-ray diffraction analysis, energy dispersive analysis of x-rays and electron-probe microanalysis. The thermodynamic properties of binary and ternary metal oxides were obtained by the solid-state galvanic cell technique incorporating oxide or fluoride solid electrolytes.

3. Major contributions

The ceramic oxide systems studied and the important results obtained are highlighted below.

3 1. *Thermodynamic studies on Fe, Co, Ni orthosilicates*

The standard Gibbs' energy of formation of 3d transition metal (Fe, Co, Ni) orthosilicates has been measured using the solid-state galvanic cells.

$$\mathrm{Pt,m + M_2SiO_4 + SiO_2//(Y_2O_3)ZrO_2//M + MO,Pt,\ M = Fe,\ Co,\ Ni,} \qquad \text{and}$$

$$\mathrm{Pt,\ Fe_3O_4 + Fe_2SiO_4 + SiO_2//(Y_2O_3)ZrO_2//Ni + NiO,\ Pt.}$$

A schematic diagram of a typical solid-state galvanic cell is shown in Fig 1 The application of CaF_2 solid

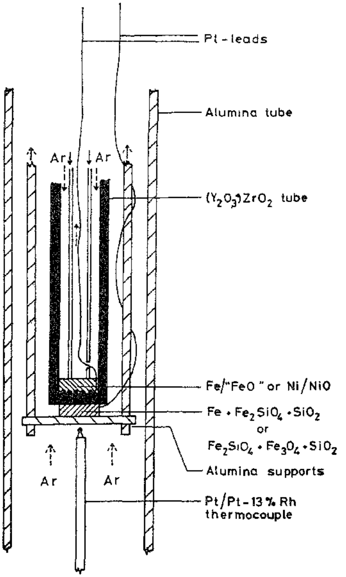

FIG. 1. Schematic diagram of cell.

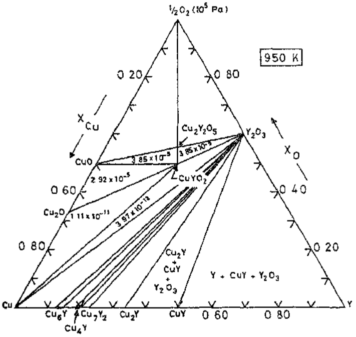

FIG. 2. Phase diagram of Cu-Y-O system at 950 K.

electrolyte for oxygen potential measurements is well documented in literature. The oxygen potential response has been attributed by Chou and Rapp[1] to the transport of dissolved oxygen in CaF_2. Ramanarayanan *et al*[2] attributed the oxygen potential response to the presence of CaO precipitates and an exchange reaction between CaF_2 and O_2 which establishes an equivalent fluoride potential at the electrodes. Since silica present in the electrode of the cell Pt,Ni + Ni_2SiO_4 + SiO_2/CaF_2/Ni + NiO, Pt is expected to react with CaO formed at the surface of CaF_2, the emf of this cell was measured as a function of time in order to elucidate the mechanism of oxygen potential response in CaF_2.

3.2. *Phase relations and thermodynamic properties of compounds in M1–M2–O (M1–M2 = Ni–Mo, Cu–Cr, Cu–Y) systems*

Phase relations and thermodynamic properties in three ternary systems of the type M1–M2–0 (M1–M2 = Ni–Mo, Cu–Cr, Cu–y) were established. Phase relations in Ni–Mo–O system at 1373 K were established by employing isothermal equilibration of several samples consisting of two- or three-phase assemblages taken in different molar ratios in evacuated and sealed quartz capsules. Thermodynamic properties of interoxides in these systems were obtained by emf method incorporating stabilized zirconia as the solid electrolyte. Based on the present results, isothermal section of Cu–Cr–0 (1150 K) and Cu–Y–O (723, 950, 1373 K) has been constructed. A section of Cu–Y–O at 950 K is shown in Fig. 2.

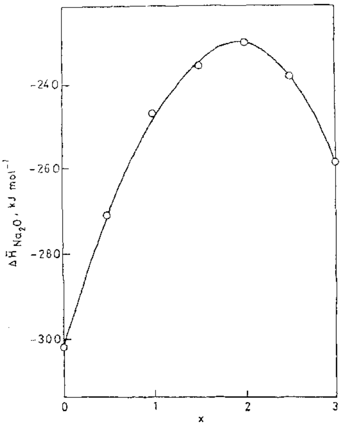

FIG 3. Variation of the partial enthalpy of Na_2O as a function of composition in the Nasican solid solution series.

3.3. *Thermodynamic studies on 2–3 spinels and their solid solutions*

Gibbs' energy of formation of Co_3O_4 from CoO and O_2 has been obtained by emf measurements. The emf measurements, high-temperature x-ray diffraction, electrical conductivity, DTA and TGA studies indicated that Co_3O_4 undergoes a second or higher order phase transition at 1120 (±20) K. This transition is associated with electronic spin unpairing in Co^{3+} ions and rearrangement of cations on the spinel lattice sites. A new value of crystal field stabilization energy (CFSE) for Co^{3+} has been calculated from the spectroscopic data. This has been used along with the CFSE of di- and trivalent Fe, Mn and Co^{2+} reported in the literature to model thermodynamic properties of mixing in Fe_3O_4–Mn_3O_4, Fe_3O_4–Co_3O_4 and Mn_3O_4–Co_3O_4 spinel solid solution systems. The activity–composition relations in $FeAl_2O_4$–$FeCr_2O_4$ spinel solid solution at 1823 K has been obtained by employing gas–solid equilibration method. Based on the results obtained in this study, it has been shown that the excess free energy of mixing is primarily due to the strain enthalpy term arising from the mixing of Al^{3+} and Cr^{3+} of differing ionic radii on octahedral site of spinel lattice

3.4. *Thermodynamic studies on Nasicon ($Na_{1+x}Zr_2Si_xP_{3-x}O_{12}$, $0 \leq x \leq 3$) and K-β-alumina*

The thermodynamic activity of Na_2O in Nasicon solid solution ($Na_{1+x}Zr_2Si_xP_{3-x}O_{12}$, $0<x<3$) has been measured as a function of temperature and composition by emf technique. The present results are consistent with the literature data for ionic conductivity[3] and cell volume[4] of Nasicon at $x = 2$. The variation of partial enthalpy as a function of composition of Nasicon solid solution is shown in Fig. 3. The activity of K_2O is α-alumina + K-β-alumina biphasic mixture has been measured as a function of temperature by employing solid-state galvanic cell technique. The present results resolve the discrepancy in high-temperature thermodynamic stability of K-β-alumina.

3.5. *Phase relations and thermodynamic properties of compounds in BaO–Y_2O_3 system*

Phase relations in BaO–Y_2O_3 system were established by isothermal equilibration method. The Gibbs' energy of formation of BaY_2O_4 and $Ba_3Y_4O_9$ from component oxides has been measured by an emf technique incorporating BaF_2+2 mol%Al_2O_3 as the composite solid electrolyte.

4. Conclusions

The major conclusions drawn based on the present investigation are summarized:

1. The third-law analysis of the standard free energy of formation of Fe_2SiO_4(ol), Co_2SiO_4(ol) and Ni_2SiO_4(ol) from component oxides and the data on oxygen potential for the fayalite–quartz–magnetite equilibrium yield temperature-independent values of ΔH°_{298}
2. The present experimental findings suggest that CaF_2 is predominantly an F^- ion conductor.
3. Only one ternary oxide, $NiMoO_4$, is present in Ni–Mo–O system at 1373 K. $NiMoO_4$ can be formed either by the oxidation of $NiO+MoO_2$ mixture or by the oxidation of $NiO+MoO_2$ mixture or by the reaction of NiO with MoO_3.
4. The isobaric section of CuO-Cu_2O-Cr_2O_3 at an oxygen partial pressure of $2{\cdot}1 \times 10^4$ Pa obtained in this study is more consistent with the thermodynamic data on interoxides than that reported by Gadalla and White[5].
5. The system Cu–Y–O contains two ternary oxides, $CuYO_2$ and $Cu_2Y_2O_5$. Based on the thermodynamic data on these two interoxides it is shown that the topology of the Cu–Y–O ternary phase diagram is sensitive to temperature.
6. The discrepancy in high-temperature thermodynamic data of Co_3O_4 is resolved with the discovery of new higher order phase-transition-coupling electronic spin unpairing in Co^{3+} and cationic rearrangement on spinel lattice.
7. The activities of component spinels in hercynite–chromite solid solution show positive deviation from ideality at 1823 K. The excess Gibbs' energy of mixing in $FeAl_2O_4$–$FeCr_2O_4$ solid solution is explained in terms of the strain enthalpy term arising from the mixing of Al^{3+} and Cr^{3+} of differing ionic radii on the octahedral site of spinel lattice.
8. The maxima in partial entropy and partial enthalpy of Na_2O in Nasicon solid solution are consistent with the maxima in ionic conductivity and cell volume at $x = 2$.
9. The discrepancy in the high-temperature thermodynamic stability of K-β-alumina reported in literature has been resolved.
10. Only two stable ternary oxides, BaY_2O_4 and $Ba_3Y_4O_9$, were detected in BaO–Y_2O_3 system. The other two ternary oxides, $Ba_4Y_2O_7$ and $Ba_2Y_2O_5$ reported by Kwestroo *et al*[6], were not detected.

References

1. Chou, S. F. and Rapp, R. A.	Electrochemical studies of dopant redoxing and diffusion at the $Pt,O_2/CaF_2$ interface, *J Electrochem. Soc* , 1983, **130**, 506–513.
2. Ramanarayanan, T. A., Narula, M. L. and Worrell, W. L.	The measurement of oxygen chemical potential with calcium fluoride solid electrolyte, *J. Electrochem. Soc* , 1979, **126**, 1360–1363
3. Tran Qui, D., Capponi, J. J. and Joubert, J. C.	Crystal structure and ionic conductivity in $Na_4Zr_2Si_3O_{12}$, *J. Solid St Chem.*, 1981, **39**, 219–229.
4. Goodenough, J. B., Hong, H Y. P. and Kafalas, J. A	Fast Na^+-ion transport in skeleton structure, *Mater Res. Bull.*, 1976, **11**, 203–220.
5. Gadalla, A. M. M. and White, J.	The system CuO–Cu_2O–Cr_2O_3 and its bearing on the performance of basic refractories in copper-melting furnaces, *Trans. Br Ceramic Soc.*, 1964, **63**, 535–552.
6. Kwestroo, W., von Hal, H. A. M. and Langereis, C.	Compounds in the system BaO–Y_2O_3, *Mater. Res. Bull.*, 1974, **9**, 1631–1638.

Thesis Abstract (Ph.D.)

Casting technology for titanium and titanium alloys—Characterisation of metal–mould reactions in zircon sand and investment moulds and evaluation of a hypoeutectic cast Ti–Si alloy by Rathindra Lal Saha.

Research supervisors: K. T. Jacob and P. Rama Rao (DMRL).
Department: Metallurgy.

1. Introduction

Titanium and its alloys have emerged as important engineeing materials in view of their high specific strength and excellent corrosion resistance. The metal is, however, costly since it requires use of high energy and complex technology to overcome problem of its highly reactive nature at higher temperatures encountered at various steps of manufacture. Casting technique is expected to provide a viable and economical route to produce near net-shaped components. However, special and costly mould materials are required to minimise metal–mould reactions for casting of titanium and its alloys[1]. It is therefore appropriate to explore methods for minimisation of metal–mould reactions which may subsequently determine economical methods for production of titanium castings. With this aim in mind, following aspects of titanium-casting technology have been studied:

(a) development of suitable zircon sand moulds with minimal metal–mould reaction,

(b) investigation of the stability of rare-earth oxides as face cost material for investment moulds, and

(c) development of low-melting cast eutectic alloy.

2. Experimental

For studying metal–mould reactions titanium rods were cast in non-consumable electrode vacuum arc furnace using drop-cast crucible, designed for the purpose, under partial pressure of argon. The same method was also used to cast hypoeutectic Ti–Si alloy pancakes using conventional water-cooled copper crucible. However, the components were cast in skull-casting attachment of a 250-kg vacuum arc furnace using consumable electrode. Graphite susceptor was used to study reactions between liquid titanium and rare-earth oxides, in isothermal condition, in a vacuum-resistor furnace.

3. Results and conclusions

3.1. *Zircon sand moulds*

Rammed graphite moulds a [illegible]sed commercially for the production of titanium castings for less critical applications. However, zirco[illegible]and can serve as cheaper substitute for graphite[2] if metal–mould reactions are minimised. In this study, sodium silicate-bonded zircon sand can serve as cheaper substitute for graphite[2] if metal–mould reactions are minimised. In this study, sodium silicate-bonded zircon sand mould system was used. The resultant mould-hardening constitutents mainly responsible for extensive reaction with liquid titanium were identified as SiO_2 and moisture. Methods to minimise effect of these constituents on metal–mould reactions have been proposed. The addition of sodium silicate was optimised (3 wt%) to obtain reasonable mould strength at a mould-firing temperature of 873 K. This condition exhibited considerable oxygen contamination (1700 ppm) in castings. The addition of 7·5 per cent ZrO_2 to the mould mix led to a decrease in oxygen contamination to 1200 ppm. However, constant increase in hydrogen in castings in both the above conditions indicated that significant amount of moisture is still present in the mould. In order to completely remove water molecules locked in silica gel network, it was found that moulds need to be fired at temperatures $\geqslant$ 1273K. Castings displayed dramatic reduction in oxygen contamination associated with moisture (60 ppm). Use of sodium aluminate as a binder further reduced contamination due to mould oxides to a low value of 40 ppm while contamination due to moisture remained unaffected. These findings were also demonstrated on two component castings.

Titanium is known to harden significantly on minor additions of interstitial solutes. It is, therefore,

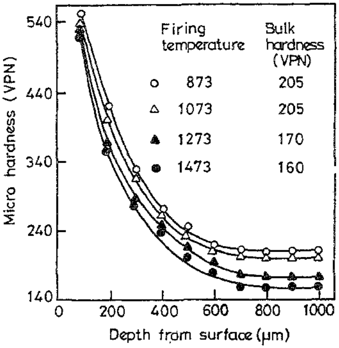

FIG 1. Effect of firing temperature on microhardness of cast rod in sodium silicate-bonded moulds containing 7·5 per cent ZrO_2

expected that microhardness profiles obtained on cast titanium rods may provide a good index for metal–mould reaction. Hardness profiles (Fig. 1) displayed two distinct regimes implying occurrence of metal–mould reaction in two steps:

(1) First metal–mould reaction takes place during filling of mould when the resulting products distribute themselves uniformly in the liquid metal because of the presence of turbulence and high diffusivity. This stage of reaction is characterised by the invariant part of the hardness profile starting at a distance of about 700 μm from the surface.

(2) Metal–mould reaction continues even after the establishment of quiescent conditions in the mould. This leads to further contamination of the surface of the casting. This diffusion zone is represented by that part of the microhardness profile which exhibits decrease in microhardness with increase in distance away from the surface.

The diffusion depth of Si and Zr, estimated from microprobe analysis, was found to be about 100 μm. This suggests that diffusion depth (700 μm) indicated by microhardness curve therefore is mainly due to oxygen.

The study showed that metal–mould reaction in titanium castings can be minimised by firing zircon sand moulds at higher temperatures and hardness profile can provide good index to relatively grade the stability of oxide base moulds Zircon sand mould system has been shown to be a viable method to cast titanium and its alloys.

3.2. *Investment moulds*

Investment mould systems used successfully for titanium castings are generally proprietary in nature. Rare-earth oxides exhibit reasonable inertness to titanium and are considered as potential candidates for face coat applications[3]. In this study, a number of rare-earth oxides along with ZrO_2 were evaluated for their relative stability against liquid titanium.

Two methods were employed to evaluate contamination levels. In one case, the experimental rods were cast in investment shells with different face coats, followed by evaluation of microhardness and bulk oxygen content to obtain relative grading of oxides. Oxygen profile was also evaluated using secondary ion mass spectroscopy (SIMS). The oxygen profile was found to follow a trend almost similar to that of microhardness profile particularly in regard to distance at which invariant portion of the curve begins. This further confirms the earlier assumption that microhardness profile can be considered to represent the oxygen profile for practical purposes. The relative grading of face coat oxides obtained in order of decreasing stability was Y_2O_3, Nd_2O_3, didymium oxide ($Nd_2O_3{\cdot}Pr_2O_3$), Sm_2O_3, Gd_2O_3, ZrO_2 and CeO_2.

In another method, the titanium rod was isothermally heated in contact with rare-earth oxides, above its melting point (1941 K) for 300 s. This method provided severe conditions for metal-mould reaction. The oxygen analysis carried out in the reacted titanium metal also provided a good index for grading of face coat oxides. Y_2O_3 exhibited least reaction followed by Nd_2O_3 and didymium oxide (Nd_2O_3. Pr_2O_3) These results are similar to those obtained with microhardness profile.

It was also observed that contamination of oxygen and metallic solute in titanium from the rare-earth oxide face coat does not correspond to their mass balance. Similar result was also obtained in zircon sand moulds which indicates that oxides do not fully dissolve in liquid titanium but oxygen from the oxides is preferentially transferred to titanium and the metallic species are left behind in the mould possibly in the form of lower oxides. Thermodynamical solubility products of Y_2O_3 and ZrO_2 were computed and compared with those of experimentally observed values. The experimental solubility product of Y_2O_3 was in good agreement with computed values, whereas results were less satisfactory with ZrO_2.

3.3. *Hypoeutectic cast alloy (Ti–6.5 wt%t Si)*

One of the methods to produce inexpensive castings is to develop low-melting eutectic alloys. This will not only lead to savings in energy consumption but would significantly reduce metal–crucible and metal–mould reactions[4]. In this study, Ti–Si system was investigated up to eutectic composition. A hypoeutectic compositioin (Ti–6·5 wt% Si) was selected for modification studies as it displayed maximum strength (840 MPa). The alloy can be of industrial importance provided its ductility (0·8 per cent elongation) can be improved. In this work, effect of minor additions of low-surface tension elements (Na, Sr, Se Te and Bi) was studied to improve ductility of the alloy.

It was observed that minor additions of Bi (0·1 wt%) resulted in two-fold improvement in ductility (1·8 per cent elongation). Differential thermal analysis (DTA) of Ti–Si–Bi alloys indicated that small additions of Bi lower the solidification temperature by about 10 K resulting in undercooling. A small increase in Si in both eutectic and dendritic regions was also observed using EPMA analysis, indicating incremental shift in Si content at the eutectic horizontal. These effects seem to be responsible for fine distribution of dendrite and eutectic regions because of increase in the number of nucleation events and increase in volume fraction of dendrite, respectively. The effect of minor addition of Bi on Ti–6·5 Si alloy therefore appears to be similar to that of Na modification of Al–Si eutectic alloy.

References

1. Eylon, D., Froes, F H. and Gardiner, R. W	*J. Metals*, 1983, **35** (2), 35–47
2 Burrus, J M. and Koch, R. K.	*Fndry Mgmt Technol* , 1982, **110** (5), 43–49
3. Lyon, S. R. and Inouye, S.	The interaction of Ti with refractory oxides, in *Titanium science and technology* (eds, R. Jaffee and H. M. Burte), 1973, pp 271–284, Plenum Press.
4 Boomberger, H. R., Hall, G S and Seagle, S. R.	Hypereutectoid Ti–Cu alloys, in *Titanium 80* (eds, H. Kimura and D. Izumi), 1980, p. 1277, TMS–AIME Publication, Warrendale.

Thesis Abstract (Ph.D.)

Thermodynamics of alloys—Theory, experiment and application by S. Srikanth.
Research supervisor: K. T. Jacob.
Department: Metallurgy.

1. Introduction

The research program reported in this work was designed to include both theory and experiment. Theoretical research was oriented towards the representation of thermodynamic data of dilute multicomponent solutions and on exploring the possibility of deriving structural details on solid and liquid alloys from the corresponding thermodynamic properties. Experiments were focussed on the measurements of activities in liquid and solid alloys by Knudsen effusion and solid-state emf technique The use of metastable equilibria for measurement of thermodynamic properties of solid alloys has been explored. A novel entropy meter for measuring partial entropy of the reactive component in an alloy has been designed. Finally, the physical chemistry of the reduction of calcia by aluminium in vacuum has been completely characterised.

2. Theoretical studies on the representation of thermodynamic properties of dilute multicomponent solutions

Different formalisms used for the representation of thermodynamic data of dilute multicomponent solutions are critically evaluated. The thermodynamic consistency of the interaction parameter formalism is analysed. Application of path-dependent integrals to the solution of the Gibbs–Duhem equation in the absence of mathematical exactness is suggested. Special relationships between interaction parameters are derived for the truncated MacLaurin series expansion for $\ln\gamma$ by solving the Gibbs–Duhem equation. A thermodynamically consistent quadratic formalism has been developed for dilute multicomponent solutions. The quadratic formalism is compared with the conventional second-order MacLaurin series representation and the relations between them are derived. The approach of Pelton and Bale[1] and Schuhmann[2] to overcome thermodynamic inconsistency of the interaction parameter formalism is discussed. It is shown that Pelton and Bale's first-order modified formalism, Schuhmann's formalism and the second-order interaction parameter formalism incorporating special relations yield identical results. The different formalisms are discussed in the light of available experimental data and their compatibility with various statistical models of solution thermodynamics is elucidated. Options available for the representation of thermodynamic data and restraints imposed by each choice of representation are discussed.

3. Volume effects and associations in liquid alloys

The associated solution model has been modified to include volume effects. The size of the complex is introduced as an explicit variable. Two approaches are considered. In the first, an analytical method is employed for determining the model parameters. The treatment is limited to A_aB type complexes and the volume of the complex cannot be determined explicitly and the thermodynamic properties are calculated from the model parameters as a function of the relative volume of the complex. The approach is limited to regular associated solutions, where the interaction energies are independent of temperature. In the numerical approach an optimisation procedure using a modified conjugate gradient method is introduced for evaluating the model parameters. In this approach, the assumption of equal atomic volumes of free atoms and temperature independence of interaction energies are relaxed and the analysis is more general, permitting the existence of complexes of the type A_aB_b. Expressions for the concentration—concentration structure factor and the liquidus in compound forming liquid alloys are deduced in terms of the parameters of the associated solution model. The analysis is applied to the thermodynamic mixing functions of liquid Ca–Al, Sb–In, Mg–Zn, Mg–Sn and Ga–Te alloys.

4. Thermodynamic measurements on liquid alloys

To explore the possibility of deriving structural information, activity measurements were carried out in a few selected complex-forming liquid alloys. Activity of calcium in liquid Al–Ca alloys ($X_{Ca} < 0{\cdot}38$) was determined by Knudsen effusion–mass loss analysis. Activity of Al in Ca-rich alloys ($X_{Ca} > 0{\cdot}44$) was

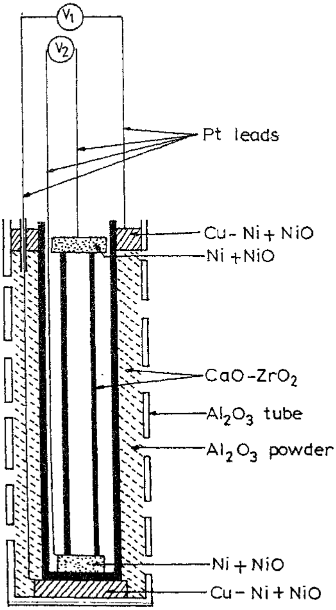

FIG. 1. Schematic diagram of the entropy meter for determining partial molar entropy of Ni in solid Cu-Ni alloys.

calculated from the measured distribution coefficient for Al between the alloy and a thin foil of pure iron, using data for the Fe–Al system reported in the literature. By combining the results of Knudsen effusion and distribution studies with the Gibbs–Duhem relation, activities of both components and integral Gibbs' energy of mixing for the complete composition range have been obtained at 1373 K. For liquid Mg–ZN alloys, vapour species effusing from a magnesia Knudsen cell containing Mg–Zn alloy at 923 K were condensed on a water-cooled copper plate. The equilibrium composition of the vapour phase over the alloy was determined from chemical analysis of the condensate. The activity coefficients of both components in the alloy were derived from the data using a modified Gibbs–Duhem relation. Activity of gallium in liquid Ga–Te alloys was measured at 1120 K using a solid-state cell incorporating yttria-doped thoria as the solid electrolyte. Activity of tellurium was derived by Gibbs–Duhem integration. The concentration–concentration structure factor derived from the experimental activities for all these alloys indicates complexing behaviour in the liquid state.

5. Thermodynamic measurements on solid alloys

The use of metastable equilibria for the determination of Gibbs' energies of solids was explored. Attempts were made to measure activities of both components in solid Ni–Co and Ni–Mn alloys at 650 K using a solid-state galvanic cell incorporating a new composite solid electrolyte. The alloy phase was equilibrated in separate experiments with fluorides of each component and fluorine potential was measured. When the difference in Gibbs' energies of formation of the fluorides was small, emf of the cell with metastable electrodes was constant for a reasonable period. In systems with large driving force for displacement reaction, the use of metastable equilibria was not fully successful.

The Gibbs' energy of formation of the intermetallic compound Au_2Na was determined in the temperature range 565–925 K using a solid-state galvanic cell employing β-alumina as the solid electrolyte. The stability of the Laves-phase Au_2Na is discussed from the viewpoint of charge transfer, size and coordination factors.

The activity of nickel in solid Cu–Ni alloys has been measured at 1000 K using a solid-state galvanic cell incorporating $(CaO)ZrO_2$ as the solid electrolyte. Partial molar entropy of nickel in solid Cu–Ni alloys has been measured directly using a newly developed twin solid-state thermocell apparatus. A schematic diagram of the entropy meter is shown in Fig. 1. A consistent set of thermodynamic data for the Cu–Ni system was derived by combining the results of the present study with selected data on enthalpy and free energy of mixing of liquid alloys and the phase diagram. The miscibility gap and the chemical spinodal boundaries obtained from the evaluated data are in good agreement with x-ray and diffuse neutron scattering studies reported in the literature.

6. Process analysis

The physical chemistry of the 'aluminothermic' reduction of CaO in vacuum is analysed. Basic thermodynamic data required for the analysis have been generated by a variety of experiments. In addition to activity measurements in liquid Al–Ca alloys, they include alloy–oxide equilibration studies in the system Ca–Al–O and measurements of the equilibrium vapour pressure of Ca corresponding to the reduction reaction:

$$6CaO(s) + 2Al(l) \rightleftharpoons 3CaO\cdot Al_2O_3(s) + 3Ca(g).$$

Auxiliary data for the Gibbs' energies of formation of calcium aluminates were taken from the literature. The various stages of reduction, the end products and the corresponding equilibrium partial pressures of calcium have been established from thermodynamic considerations.

References

1. Pelton, A. D. and Bale, C. W.	*Metall. Trans. A*, 1986, 17, 1211–1215.
2. Schuhmann, R. Jr	*Metall. Trans. B*, 1985, **16**, 807–813

Thesis Abstract (Ph.D.)

Phase transformations in Ti–N and Ti–Fe–N alloys and superconductivity by D. Sundararaman.
Research supervisors: S. Ranganathan and V. S. Raghunathan.
Department: Metallurgy.

1. Introduction

It is well known that mechanical and physical properties of titanium and its alloys are dependent sensitively upon the presence of interstitial elements like carbon, nitrogen and oxygen[1]. Among these, nitrogen is an effective stabiliser of the hexagonal closepacked α-titanium, in addition to imparting maximum strength to titanium and its alloys. The Ti–N system has not been studied in detail as compared to Ti–O and Ti–C systems[2,3]. Considering the atom size of nitrogen solute against the typical octahedral void size of α-titanium, there exists a certain probability of distortion of the host lattice. Consequent strain energy contribution influences the overall stability of the various phases that could form in Ti–N system by various decomposition processes. The increase in the strain energy of the lattice caused by the occupation of interstitials results in two significant effects: (i) nitrogen solubility is severely restricted and (ii) even with the low solubility an ordering of nitrogen in the lattice is favoured. The present study is aimed at understanding the ordering of nitrogen atoms in hcp titanium and the subsequent precipitation of TiN_x (α′) tetragonal phase from the supersaturated matrix. Further, the study has been extended to examine the role of nitrogen on the phase transformations that occur in binary Ti–Fe alloys.

2. Experimental procedures

Thin foils of 25–50 μm thickness of titanium, Ti-2 a/o, 6 a/o Fe were nitrided in flowing ultra-high purity nitrogen gas in the α-phase fields and quenched from the β-phase regions of the respective alloys. Some of the Ti–1·6 a/o N alloy samples were aged in the temperature interval 300–673 K for various durations extending up to 50 hours. Both the quenching and ageing treatments were done in a vacuum better than 10^{-3} Pa. T_c measurements were carried out for both quenched and aged conditions of Ti–N alloys resistively using a four-probe technique in a conventional liquid helium exchange gas cryostat. Both conventional transmission electron microscopy and high-resolution electron microscopy were carried out to characterise the phase transformations occurring in the systems.

3. Nitrogen ordering—a theoretical approach

The energetics of interstitial ordering has been analysed using a quasi-chemical approach incorporating interactions up to second nearest neighbours[4,5]. A nitrogen housing scheme has been proposed with a view to minimise the strong coulombic repulsion and to offer minimum lattice distortions. Modelling on this basis, it is found that the combined effect of first and second near-neighbour interactions gives rise to the formation of ordered superstructures. A martensitic transformation of the ordered domains is predicted around the composition of 16 a/o nitrogen, as a result of the stress field associated with the interstitial atoms[6].

4. Phase transformations in Ti–N and Ti–Fe–N alloys

4.1. *Ti–N alloys*

The early stages of the decomposition of the supersaturated α″ phase which was obtained on quenching the Ti–1·6 a/o N alloy have been found to be associated with a tweed constrast indicative of early stages of precipitation[7] (Fig. 1). The tetragonally ordered α′ phase formed from α″ by continuous ordering transforms to incoherent Ti_2N precipitates on ageing in the temperature range 323–673 K. While no perceptible growth of homogeneously transformed α′ phase is observed in the matrix, lath boundary precipitation of α'/Ti_2N occurs during low-temperature ageing ($T < 373K$). On ageing at high temperatures ($T > 373K$), both matrix and lath boundary precipitation of Ti_2N take place uniformly by nucleation and growth process.

The orientation relationship between the α″ and α′ phases has been identified as

$$(1\,0\,\bar{1}\,0)_{\alpha''} \parallel (0\,1\,1)_{\alpha'}$$
$$[1\,\bar{2}\,1\,0]_{\alpha''} \parallel [0\,1\,\bar{1}]_{\alpha'}.$$

The experimental results obtained on the precipitation of Ti_2N from supersaturated α″ phase suggest that the transformation $\alpha'' \rightarrow TiN_X$ ($X \sim 0{\cdot}2-0{\cdot}5$) has been shown to satisfy the invariant plane strain conditions (IPS)[8]. The lattice correspondence between α and α′ phases is as shown in Fig. 2.

High-resolution images were obtained in both the quenched and aged samples of the Ti–1·6 a/o N alloy. Images shown in Fig. 3 have been interpreted using the geometrical projection of atoms[9] from the anti-rutile Ti_2N structure. On comparing the simulated and actual high-resolution image it is concluded that

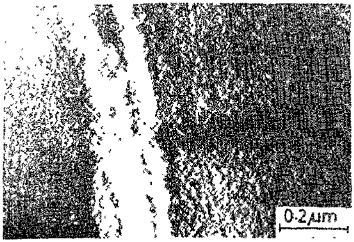

FIG 1 Electron micrograph of a typical region which had undergone a pre-precipitation reaction Tweed contrast is indicative of the local formation of nitrogen-rich zones

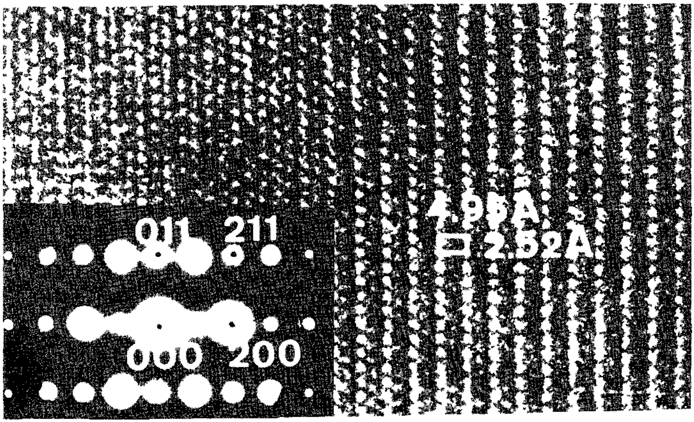

FIG 2. High-resolution structure image of the ordered α′ phase in the quenched sample. The white dots correspond to the Ti atom configurations in the anti-rutile structure. Inset shows the SAD pattern used to obtain the image

only Ti atoms are imaged as white dots. The interfaces between the α/α′ phases remain coherent in the quenched condition of the alloy, while they become incoherent on continuous precipitation of nitrogen atoms, from the matrix.

It is inferred that the disordered supersaturated α″ transforms to Ti_2N by the following predominant reaction sequences

(i) $\alpha'' \rightarrow \alpha + \alpha' \rightarrow \alpha + Ti_2N$ by continuous ordering at $T \leq 473$ K;

(ii) $\alpha'' \rightarrow \alpha + Ti_2N$ by heterogeneous nucleation and growth at $T > 473$ K.

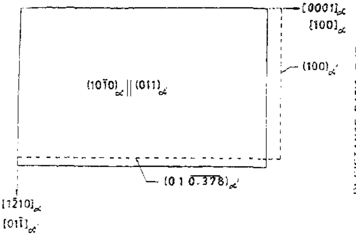

Fig. 3 Lattice correspondence between the α-matrix and the α′product phase

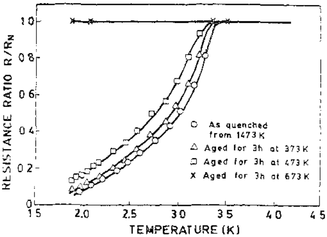

Fig. 4 Resistivity behaviour of a Ti–2 a/o N alloy at very low temperatures for various thermal treatments

4.2. *Ti–Fe–N alloys*

In a concurrent study, Ti–Fe (2 and 6 a/o Fe) alloys have been investigated to understand critically the nature of martensitic and omega reactions. In the light of the studies in Ti–N system, it is expected that nitrogen solute would have a significant influence on these reactions. Optical metallography revealed the presence of hexagonal α_1' phase in a matrix of retained β phase on quenching the Ti–6 a/o Fe alloy. The hexagonal α_1' phase exhibited two distinct morphologies, one obeying Burger's orientation relation and the other not conforming to any specific orientation relation The retained β phase showed the existence of dynamical omega fluctuations[10] as well as the presence of fine-scale omega phase precipitation The nitrogen bearing Ti–6 a/o Fe alloy on quenching at comparable rates produced only Burger's oriented martensite plates and no retained β phase could be detected. In other words, the nitrogen addition seems to inhibit the $\beta \rightarrow \beta + \omega$ reaction while promoting the $\beta \rightarrow \alpha_1'$ reaction[11].

Many of the nitrogen martensite colonies in both the Ti–2 a/o Fe–2 a/o N and Ti–6 a/o Fe–1·5 a/o N *alloys have shown signs of initial stages of decomposition, exhibiting features similar to that obtained in* Ti–1·6 a/o N alloy. Electron diffraction analyses confirm that the product microstructure possesses the tetragonal Ti_2N structure. The experimental observations along with the theoretical predictions on nitrogen-ordering behaviour suggest that the reactions in interstitial alloys proceed frequently stepwise till it reaches equilibrium composition In the process, the system minimises the total energy by local rearrangements to form a variety of metastable ordered phases

5. Resistivity and superconductity studies in Ti–N alloys

It is well known that titanium, on quenching from the β-phase regions, does not show superconducting transition down to 1·6K Interestingly, all the titanium–nitrogen alloys exhibited enhancement in supercon*ducting transition temperature T_c and for any concentration up to 2 a/o N, T_c is at its highest value in* the β-quenched state of the alloy, *i e*, ~ 3K. It has been noticed that a degradation in T_c occurs due to ageing the alloy at higher temperatures It has been found that the samples are restored to normal state after 10 hours of ageing at 473K. Resistivity measurements for various treatments have been illustrated in Fig. 4. Thus, it is demonstrated that the superconducting parameter T_c is sensitive to microstructure. The phenomenon investigated was examined in detail from various angles like nitrogen ordering, precipitation behaviour and microstructural characteristics and the findings of the examination are adopted to provide a physical basis for the observed superconductivity in dilute nitrogen alloys of titanium Well-known mechanisms like the proximity effect[12] and the effect of dislocations do not satisfactorily explain the observed enhancement of T_c. Various other approaches/models like Kulik layer model[13] and retained β effect were also examined for explaining the phenomenon. In the absence of a satisfactory explanation from the existing approaches/models, a new approach has been proposed, namely, the 'strain-field criterion', to explain the superconductivity behaviour The strain-field criterion suggests that the strain-field distribution associated with the precipitate/matrix interfaces could be responsible for the enhanced T_c. The strain-field dependence on ageing has to be taken into account while interpreting the anomalous behaviour of superconductivity The high-resolution electron microscopy work carried out in the Ti–1·6 a/o N alloy lends support to the above-mentioned view.

6. Conclusions

The major conclusions of the work are summarised below:

(1) Theoretical studies on the energetics of the ordering of N-atoms and precipitation indicate that there exists a critical concentration around 16 a/o N beyond which hexagonal structure of α-Ti is rendered unstable.

(2) The structural transformation from hexagonal to tetragonal (anti-rutile structure) takes place martensitically and the microscopic strain associated with the transformation $\alpha'' \rightarrow TiN_X$ ($X \sim 0{\cdot}2-0{\cdot}5$) is shown to satisfy the IPS conditions.

(3) Precipitation of the second phase in Ti–Fe–N alloy with a tetragonal structure follows a similar sequence observed in dilute Ti–N alloys.

(4) The actual T_c values have been found to be strongly dependent upon the N-concentration and microstructure. The strain-field criterion suggests the dependence of T_c on the nature and distribution of the strain-field patterns in and around the coherent interphases of α and α′. When the strain-field interaction ceases to be long range in nature, degradation in T_c is noticed.

References

1. Magnitzkii, O N.	In *Titanium science and technology* (eds, R I Jaffee and H. M Burte), Vol. 3, p 1915, 1973, Plenum Press
2. Yamaguchi, S	*J Phys Soc Jap* , 1969, **27**, 155–163.
3. Moisy Maurice, V , Lorenzelli, N , De No Vion, C H and Convert, P.	*Acta Metall.*, 1982, **30**, 1769–1779
4 McLellan, R B. and Dunn, W W	*J Phys. Chem Solids*, 1969, **30**, 2631–2637.
5 Guggenheim, E A.	*Mixtures*, 1952, Clarendon Press
6 Sundararaman, D., Raju, S and Raghunathan, V S.	*J. Phys. Chem Solids*, 1989, **50**, 1101–1112
7 Sundararaman, D., Terrance, A L. E., Seetharaman, V and Raghunathan, V. S.	*Trans. JIM*, 1983, **24**. 510.
8. Kelly, A. and Groves, G W	*Crystallography and crystal defects*, 1970, p 321, Addison Wesley.
9. Cowley, J M	*Diffraction physics*, 1975, p. 279, North-Holland.
10. de Fontaine, D., Paton, N. E and Williams, J. C	*Acta Metall.*, 1971, **19**, 1153–1162.
11. Sundararaman, D., Mohandas, E. Raghunathan, V. S. and Ranganathan, S	*Trans IIM*, 1987, **40**, 249–257.
12 Deutscher, G. and Degenues, P. G.	*Superconductivity* (ed , R. D. Parks), Vol. 2, pp 1005–1034, 1969, Marcel Dekker
13. Kulik, I. O	*Solid St. Commun.*, 1976, **19**, 535–537.

Thesis Abstract (Ph.D.)

Numerical and analytic studies of generalised Burgers equations by K. R. C. Nair.
Research supervisors: P. L. Sachdev and V. G. Tikekar.
Department: Mathematics.

1. Introduction

The Burgers equation (BE) $u_t + uu_x = (\delta/2)u_{xx}$, $\delta > 0$ represents nonlinear wave motion in a diffusive medium It describes a balance between nonlinear convection and (small) viscous diffusion. However, mathematical models such as those representing nonlinear wave motion in acoustics, electromagnetism, etc., are not so simple. This is because of their geometric spreading and material inhomogeneity. BE is linearisable through Cole–Hopf transformation to the heat equation. The generalised Burgers equations (GBEs), in general, do not admit linearisation. Perturbation methods have been extensively used by several investigators for solving GBEs, but these solutions are valid only over restricted space–time regions. Asymptotic methods are very powerful tools for solving differential equations; but the solutions usually involve arbitrary constants or result in the solution of the original equations on different scales. Numerical solutions are real genuine solutions which may be obtained over the entire space–time range; numerical methods pose severe difficulties especially when the initial function is discontinuous[1].

2. Numerical and analytical investigation

The present study is aimed at devising numerical methods for solving GBEs with continuous or discontinuous initial profiles and finding analytic solutions for certain space–time domains. A uniform characterisation of the GBEs by relating them *via* similarity transformations to a second-order nonlinear ordinary differential equation (ODE) which we refer to as generalised Euler-Painleve equation (GEPE) is also conceived. This is similar to the Painleve property for the Korteweg–de Vries (KdV) type of nonlinear dispersive wave equations.

A hybrid numerical scheme is devised by adopting pseudospectral and predictor–corrector implicit finite difference methods and is employed for solving GBEs[2]. This scheme is first validated with the known analytic solution of the BE. For the nonplanar BE

$$u_t + uu_x + Ju/(2t) = (\delta/2)u_{xx}, \; J = 1,2$$

the numerical computations are carried out all the way from a sawtooth initial profile to the final decay *via* embryonic shock, Taylor shock, thick shock and old age. For the cylindrical case we have a generalised similarity form of solution, motivated by known analytic form for the plane case, leading to an explicit analytic determination of the Reynolds number. The analytic (asymptotic) form of the Reynolds number for nonplanar cases is completely determined by finding the constants from the numerical solution.

The evolution and decay of cylindrical and spherical nonlinear acoustic waves generated by a sinusoidal source is governed by

$$V_R - VV_\theta = \epsilon g(R)V_{\theta\theta}$$

with $g(R) = 1$, $R/2 + R_o$, and $\exp(R/R_o)$ for plane, cylindrical, and spherical symmetries, respectively. e and R_0 are two nondimensional parameters. The analytic solutions of this GBE for $g(R) = 1$ (plane BE) were first reproduced numerically. This has helped to demarcate various regimes over which different analytic solutions—inviscid (Fubini), sawtooth, composite, Fay, and old age—hold. For the nonplanar cases, numerical solutions are found to agree excellently with the analytic (asymptotic) results[2]. For the canonical problem of the cylindrical Burgers equation, treated by Enflo, the old age constant was determined numerically and found to be in good agreement with his estimate of the same. The saturation phenomenon—the amplitude of the final old age wave becoming independent of the amplitude of the wave at the source—for the cylindrical case, is also demonstrated. An interesting feature of the numerical solution is the re-emergence of the symmetry of the solution about the maximum of the amplitude in the old age. The evolution of the waves for different source geometries is depicted graphically[3]. We have investigated GBE *via* similarity transformations to discover their characterisation and identification by the GEPE

$$YY'' + ay'^2 + f(x)yy' + g(x)y^2 + by' + c = 0$$

in the same way as Painleve equations characterise KdV type of equations. Here, *a*, *b*, and *c* are real constants and $f(x)$ and $g(x)$ are smooth functions. We treated the following GBEs of physical interest for the study mentioned above[4]:

$$u_t + u^P u_x = (\delta/2)u_{xx}, \; p > 0; \qquad (1)$$

$$u_t + u^p u_x = (\delta/2)\,(1+t)^n u_{xx},\ p > 0; \tag{2}$$

$$u_t + u^p u_x + (Ju/2t) = (\delta/2) u_{xx},\ p > 0 \tag{3}$$

For $p = 1/(J+1)$, $J = 1, 2$ we are able to get an exact one parameter family of solutions in terms of exponential and error functions for eqn (3) and for $p = p_n = (1-n)/(1+n)$ for eqn (2).

References

1. Sachdev, P L	*Nonlinear diffusive waves*, 1987, Cambridge University Press.
2. Sachdev, P L., Tikekar, V. G and Nair, K R C.	Evolution and decay of spherical and cylindrical N waves, J Fluid Mech., 1986, **172**, 347–371
3. Sachdev, P L. and Nair, K R. C.	Evolution and decay of cylindrical and spherical nonlinear acoustic waves generated by a sinusoidal source, *J. Fluid Mech* , 1989, **204**, 389–404
4. Sachdev, P. L , Tikekar, V G and Nair, K R C	Generalised Burgers equations and Euler–Painleve transcedents-III, *J Math Phys* , 1988, **29**, 2397–2404

Thesis Abstract (Ph.D.)

Studies of doping effects in the binary liquid system aceto-nitrile + cyclohexane and the development of associated instrumentation by B. Ravi Gopal.
Research supervisors: E. S. Raja Gopal and V. C. Vani.
Department: Physics.

1. Introduction

Many physical systems exhibit phase transitions culminating in a critical point. The system undergoes a second-order phase transition wherein the first derivative of the free energy with respect to volume, entropy, etc., is continuous[1]. A few well-known examples are that below the critical temperature, fluids separate into liquids and vapour, certain fluid mixtures into two phases with differing compositions, ferromagnets spontaneously magnetize, ferroelectrics develop a polarisation, liquid helium becomes a superfluid and certain metals and their alloys become superconducting.

Binary liquids are two-component liquid mixtures of polar + nonpolar, weak acid + water, weak base + water or polymer + poor solvent types[2,3]. They exhibit complete miscibility above the upper solution critical temperature and phase separate into two coexisting phases below T_c. The interest in the critical phenomena of binary liquid systems is largely due to the fact that the critical temperature is more easily accessible than in any other system[2,4]. Major experimental quantities of investigative interest near the liquid–liquid T_c involve phase diagram, correlation length, specific heat, osmotic susceptibility, shear viscosity, interfacial tension and electrical transport properties.

The binary liquid system cyclohexane and acetonitrile at the critical concentration is chosen for the study under the effect of two dopants—water and acetic anhydride. Its coexistence curve has been studied earlier[5]. This system is characterised by a very small density difference of the order of 1 part in 500 at 20°C, with acetonitrile being the heavier liquid at this temperature. The thermal expansion coefficients of cyclohexane and acetonitrile, being $0{\cdot}00120\text{K}^{-1}$ and $0{\cdot}00138\text{K}^{-1}$, respectively, indicate that there is a density crossover or a density inversion at a temperature of ≈34°C called the density inversion temperature t_i. This work is primarily concentrated on the density inversion characteristics and the interfacial tension variation due to the addition of dopants. Further, precision thermal and electronics instrumentation developed is also discussed.

2. Thermal and electronic instrumentation

The experiments have been carried out in a thermostat with 10 litres of liquid paraffin as the thermostatic fluid. Mechanical stirrers ensure temperature homogeneity The heat input is *via* immersion heaters supplied with low-voltage dc. Thermal insulation using ceramic wool aided by an active thermal barrier which forms a 40 ±1°C shield serves to minimise ambient temperature variation effects on the thermostatic fluid.

Analog control has been chosen for the present temperature-controller design. The PID principle offers excellent undershoot and overshoot minimisation in addition to allowing control near zero-error levels. The preamplifier is designed using MP221 chopper amplifier hybrid module. The P, I and D stages have been implemented with LM725 instrumentation OP amps. The overall control stability achieved has been ±1mK over time periods of the order of 72 to 100 hours.

Temperature readings during the course of the experiments have been recorded with resolutions of 0·26 mK using resistance thermometric methods. The sensor used is a platinum-resistance element. The element's resistance was measured by a $6^1/_2$ digit programmable Keithley model 1923 multimeter with an IEEE–488 interface and four-lead resistance measurement capability. The 1923 was interfaced to a PC/XT using the IEEE–488 bus. The instrument control software developed is capable of accepting user-defined constants in the Callendar–van Dusen equation relating resistance to temperature.

Power shutdowns in the laboratory have unfortunately been a common feature and conventional backup power sources did not qualify to meet the requirements in one way or the other. For this reason, a low-cost, high-reliability and high-stability uninterrupted power source employing pulse width modulation has been designed and fabricated. The load regulation achieved has been ≈1·3 per cent and the efficiency is better than 85 per cent.

3. Experimental

As mentioned earlier, there is a density inversion in the present binary system around 34°C. The addition of a dopant in small quantities has an effect on the t_i of the system and on other physical parameters. The doping with water and with acetic anhydride changes the initial density of the component phases and thus alters t_i. Experiments have been performed to determine the inversion temperatures at different concentrations of the dopants. A simplified model for the rate of change of t_i with dopant quantity for both the cases of doping has been presented[6]. This model assumes that (i) the volumes of mixing are zero, (ii) the thermal expansion coefficients of the individual phases are not altered due to the addition of the dopant, and (iii) the densities of cyclohexane- and acetonitrile-rich phases, due to their mutual solubilities, are altered in a weighted manner. The experimental results agree well with the simplified model. High-resolution proton nmr spectroscopy has been used to estimate the partition coefficient k of an impurity between two liquid phases.

Two other physical quantities that undergo a change with doping are the critical temperature and the interfacial tension. Theories predict[7,8] that impurities which increase T_c are surface inactive and increase the value of the interfacial tension σ, while surface-active agents that decrease T_c also decrease σ. Experiments have been performed at different concentrations of both water and acetic anhydride and the results have been presented to verify the theoretical predictions while making comparisons with previously quoted data for the undoped system[9]. The value of the critical exponent μ of surface tension for both the doping cases has been evaluated with a least square fit of the experimental data. $\mu = 1{\cdot}26 \pm 0{\cdot}03$ does not show very appreciable shift due to doping, which is in accordance with theory. The value of σ shows a shift in the positive direction with water doping as does the value of T_c. The data are analysed with the assumption that the volume of mixing is zero. There is a decrease in the value of the interfacial tension and T_c due to acetic anhydride doping. Figure 1 is a plot of σ *vs* temperature for the undoped and doped cases. This is in good accordance with theoretical predictions. In the relation $\sigma = \sigma_0(-t)^\mu$, however, the value of the amplitude σ_o undergoes a decrease from around 77 dynes/cm to around 42 dynes/cm in the case of water doping with 0·01 wt % of water with respect to acetonitrile and to approximately 13 dynes/cm in the case of acetic anhydride doping with 0·042 wt % of acetic anhydride with respect to acetonitrile.

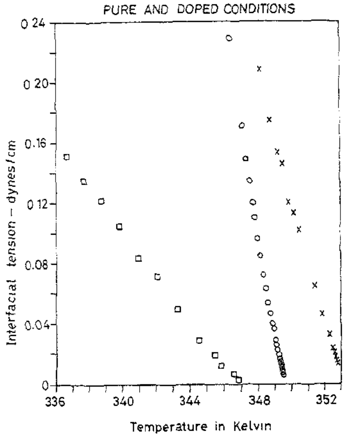

□: Acetic anhydride; x: Water; o: Pure.

FIG. 1. α *vs* Temperature

References

1. STANLEY, H. E. — *Introduction to phase transitions and critical phenomena*, 1971, Clearendon Press
2. KUMAR, A., KRISHNAMURTHY, H. R., AND GOPAL, E. S. R. — *Phys. Rep.*, 1983, **98**(2), 59–143
3. ROWLINSON, J. S. AND SWINTON, F. L. — *Liquids and liquid mixtures*, 1982, Butterworths Scientific
4. SENGERS, J. V. AND LEVELT SENGERS, J. M. H. — *A. Rev. Phys. Chem.*, 1986, **37**, 189–222.
5. VANI, V., GUHA, S. AND GOPAL, E. S. R — *J. Chem. Phys.*, 1986, **84**, 3999–4007.
6. RAVI GOPAL, B., VANI, V. C., GUHA, S. AND GOPAL, E. S. R. — *J. Phys. III*, 1991, **1**, 639–650.
7. RICE, O. K. — *J. Chem. Phys.*, 1976, **64**, 4362–4367.
8. SEMENCHENKO, V. K. — *Russ. J. Phys. Chem.*, 1982, **56**, 626–627.
9. GUHA, S., VANI, V. C., JAYALAXMI, Y. KUMAR, A., RAVI GOPAL, B. AND GOPAL, E. S. R. — *J. Solution Chem.*, 1987, **16**, 691–697.

Thesis Abstract (Ph.D.)

Investigations of molecular interactions by photoelectron and electron energy loss spectroscopies by T. Pradeep.
Research supervisors: C. N. R. Rao and M. S. Hegde.
Department: Solid State and Structural Chemistry Unit.

1. Introduction

Though the literature abounds with information on the thermodynamic and structural aspects of molecular complexes, there has been no systematic effort to understand their electronic structures[1]. Electron spectroscopic techniques such as ultraviolet photoelectron spectroscopy (UVPES) and electron energy-loss spectroscopy (EELS) provide unique means of obtaining direct information on the electron states of these systems. First part of this work involves the study of several donor–acceptor complexes and of van der Waals molecules by the HeI photoelectron spectroscopy in the vapour phase. Electron energy-loss investigation of the electronic transitions of molecular complexes constitutes the second part of the work. The results are discussed in the light of *ab-initio* quantum chemical calculations.

2. Experimental

Indigenously designed and fabricated photoelectron (PE) and electron energy-loss spectrometers[2-4] were employed in this investigation. Generally, the samples were prepared by co-condensing the donors with equal amounts of acceptors in a glass ampoule under vacuum. Dimers of alcohols, carboxylic acids and the van der Walls molecule Xe...HCl were studied with the use of molecular beams. Features due to the free donor or the acceptor molecules were present in many of the systems and these were removed by spectrum stripping. Molecular orbital (MO) calculations were carried out with the Gaussian 86 system of programmes[5] using the STO-3G, 3-21G and 6-31G* basis sets.

3. Results and discussion

The results of the investigations of electronic structures of a variety of electron donor–acceptor complexes, hydrogen-bonded systems and van der Waals molecules by employing ultraviolet (HeI) photoelectron spectroscopy are presented in Part I along with results from MO calculations. In the complexes of BH_3 with H_2S and H_2O the highest occupied molecular orbitals are BH_3 derived[6]. The PE spectra of the strong adducts of BF_3 with H_2O, CH_3OH, $(C_2H_5)_2O$ and CH_3CN as well as of weak complexes of BF_3 with NO, H_2S and $(C_2H_5)_2S$ show that the ionization energies of the fluorine lone pair orbitals of BF_3 are shifted in proportion to the strength of the donor–acceptor interaction[7]. BF_3 seems to form a contact pair with CS_2. HeI spectra of the 1:1 adducts of $AlCl_3$ and $GaCl_3$ with $(C_2H_5)_2O$ and $(C_2H_5)_2S$ are similar to those of BF_3 complexes. HeI photoelectron spectra of complexes formed by SO_2 with the electron donors trimethyl amine, triethyl amine, diethyl ether and diethyl sulphide show that the shift in the ionization energy of the lone pair orbital of the donor in these complexes varies proportionally with the binding energy as well as the magnitude of charge-transfer to SO_2[8]. Some of the SO_2-acceptor systems were also investigated. Based on these investigations, the energy-level diagrams of the complexes of BH_3, BF_3 and SO_2 have been constructed.

Hydrogen-bonded complexes $(C_2H_5)_2O$. HCl and SO_2. HCl show marginal shifts in the ionization energies of the constituents. Photoelectron spectra of the dimers of methanol and ethanol obtained by employing the molecular-beam photoelectron spectrometer could be assigned on the basis of the orbital ordering predicted with a linear hydrogen-bond geometry. The photoelectron spectrum of the van der Waals molecule Xe....HCl shows that while the ground state ion is bound with a dissociation energy of 3·34 eV, some of the excited ionic states are repulsive[9].

Electron energy-loss spectroscopic studies of the electronic transitions of electron donor–acceptor complexes, hydrogen-bonded complexes and other systems in vapour phase are presented in Part II. The energy losses are assigned to various transitions based on experimental orbital energies and quantum chemical calculations. The molecular complexes studied are $BH_3.H_2S$, $BH_3.CO$[5] and $BF_3.H_2S$[6]. Vacuum ultraviolet transitions of $AlCl_3$, $AlBr_3$ and $FeCl_3$ have been obtained by means of vapour-phase EELS. Electronic transitions of Fe_2Cl_6 are also discussed Electron energy-loss spectra of the complexes of SO_2 with $(C_2H_5)_3N$, $(C_2H_5)_2O$ and $(C_2H_5)_2S$ have been obtained in vapour phase. Only the amine–SO_2 complex shows a band ascribable to the charge-transfer transition.

Electronic transitions of diethyl ether–HCl and SO_2.HCl complexes show small shifts from those of HCl and the free electron donors as expected of weakly interacting systems[3]. Electronic spectra of the dimers of formic and acetic acids are markedly different from those of the monomers. Dimers show characteristic $n \rightarrow \pi^*$ and $\pi \rightarrow \pi^*$ transitions in the 7–11 eV region. Based on the results from HeI photoelectron and electron energy-loss spectroscopic investigations, the complete molecular orbital schemes of $BH_3.H_2S$, $BF_3.H_2S$ and the dimers of carboxylic acids have been constructed.

References

1. Rataczak, H. and Orville-Thomas, W. J (eds) *Molecular interactions*, Vols 1–2, 1981, Wiley
2. Jayaram, V and Hedge, M S. *Proc Indian Acad Sci Chem Sci*, 1986, **97**, 617–626.
3. Pradeep, T. and Hegde, M S *Proc Indian Acad Sci. Chem Sci*, 1991, **103**, 591–597
4. Hegde, M. S., Jayaram, V, Kamath, P. V and Rao, C. N. R. *Pramana*, 1985, **24**, 293–310
5. Frisch, M, Binkley, J S, Schelegel, H B, Raghavachari, K, Melius, C F., Martin, R. L, Stewart, J. J P., Bobrowicz, F. W., Roholfing, C M, Khan, L. R., Fox, D. J, Fleuder, E M and Pople, J. A *Gaussian* 86, 1984, Carnegie Mellon Quantum Chemistry Publishing Unit, Pittsburg, PA.
6. Pradeep, T., Sreekanth, C S., Hegde, M. S. and Rao, C. N R. *J Mol Struct.*, 1989, **194**, 163–170
7. Pradeep, T., Sreekanth, C S, Hegde, M. S. and Rao, C N. R. *Chem Phys Lett*, 1988, **151**, 499–502
8. Pradeep, T, Sreekanth, C S, Hegde, M. S. and Rao, C. N. R. *J. Am Chem. Soc*, 1989, **111**, 5058–5063.
9. Pradeep, T., Hegde, M. S., and Rao, C. N. R. *J Chem Phys*, 1991, **94**, 4680–4681

Thesis Abstract (Ph.D.)

Electron spectroscopic investigations of the interaction of O_2 and CO with clean and modified transition metal surfaces and of superconducting cuprates by M. K. Rajumon.

Research supervisors: C. N. R. Rao and M. S. Hegde.

Department: Solid State and Structural Chemistry Unit.

1. Introduction

Techniques of electron spectroscopy have been most useful in the investigation of the electronic structure of solids and the interaction of gas molecules with various solid surfaces[1,2]. Basically, these techniques involve kinetic energy analysis of the electrons ejected due to the impact of photons or electrons. The basic energy balance equation for this process is

$$h\nu = E_b + E_k + O$$

where $h\nu$ is the photon energy, E_b the binding energy of the level from which the electron is ejected, E_k the kinetic energy of the emitted electron and O the work function of the spectrometer. The most commonly used methods are x-ray photoelectron spectroscopy (XPS), ultraviolet photoelectron spectroscopy (UPS) and Auger electron spectroscopy (AES). To study the vibrational modes of the adsorbed atoms, electron energy-loss spectroscpy (EELS) is employed. Here, a low-energy electron beam (~5 eV) is allowed to interact with the surface and the loss in energy of the primary beam gives information about the vibrational modes of the adsorbent surface as well as the adsorbed species. The work primarily deals with the study of adsorption of O_2 and CO with clean and modified transition metal surfaces as well as simulated catalysts prepared *in situ* in the electron spectrometer. In addition, electron spectroscopic studies have been carried out on some interesting high T_c superconducting cuprates.

2. Results and discussion

Adsorption of oxygen has been studied on the (100), (110) and (111) surfaces of Ag, Cu and Ni employing XPS and UPS[3]. Besides atomic species with a O(1s) binding energy of 530 eV, molecular adsorption is found on all the three Ag surfaces associated with a characteristic O(1s) binding energy at 532 eV. HeII spectra show a feature around 3 eV due to the molecular species. Molecular adsorption is also found on all the three surfaces of Cu with a characteristic binding energy of 533 eV. The proportion of molecular species is maximum on the (111) surfaces and least on the (110) surfaces of both Ag and Cu. On Ni surfaces there is no molecular adsorption; a unique O(1s) feature ascribed to O^{1-} species is found at 531 eV. The intensity of this feature does not vary significantly with temperature in contrast to the O(1s) feature due to the molecular species on the Ag and Cu surfaces.

Changes in the valence band and the core levels of Al-promoted Ni and Cu surfaces and the interaction of CO and O_2 with these surfaces have been investigated using XPS, UPS, AES and vibrational EELS techniques. Interaction of O_2 with such modified surfaces gives rise to Al_2O_3 leaving behind the transition metals unaffected[4]. CO adsorbed on Al-promoted Ni and Cu surfaces undergoes facile dissociation at 300K or below[5]. A precursor molecular state, with a large separation between the 4σ and the 5σ orbitals is observed when CO is adsorbed on Al-promoted Ni and Cu surfaces. An unusually low C–O stretching frequency at 1300 cm^{-1} is observed on the Al-promoted Ni surface. The satellites observed in the photoelectron spectra of CO adsorbed on a clean Cu surface are absent on the Al-promoted Cu surface.

Adsorption of CO on Ni-deposited Ti and Nb surfaces, around 300K, is dissociative compared to the clean Ni surface where it is molecular[6]. On a clean Ti or Nb surface, however, adsorption of CO is molecular at 80K with a large separation between the $(1 + 5\sigma)$ and the 4σ orbitals. This precursor state dissociates well below 300 K. Core-level spectra in the C(1s) and O(1s) regions also support these observations.

The catalytic and chemisorptive properties of transition metals can be greatly modified by supporting these metals on various substrates like TiO_2 and Al_2O_3. Interaction of CO with Ni/Al_2O_3 and Ni/TiO_2 surfaces prepared *in situ* in the electron spectrometer has been investigated by UPS and XPS[6,7]. Adsorption of CO on these surfaces is dissociative at 300K unlike on a clean Ni surface where it is molecular at this temperature. On a high-temperature-annealed Ni/TiO_2 surface, CO is dissociatively chemisorbed even at 80K, unlike on Ni/Al_2O_3 and nonannealed Ni/TiO_2 surfaces where CO is molecularly chemisorbed. These observations suggest that strong metal support interaction (SMSI) can be induced in Ni/TiO_2 by high-temperature annealing.

Core-level photoelectron spectroscopic studies have also been performed on $Tl_2Ca_{n-1}Ba_2Cu_nO_{2n+4}$, $TlCa_{1-x}Nd_xSr_2Cu_2O_7$ and $Bi_{1.5}Pb_{0.5}-(Ca,Sr)_{n+1}Cu_nO_{2n+4}$ which are all hole superconductors[8]. The Cu $2p_{3/2}$ spectra show that there is no Cu^{3+} in these cuprates. There is substantial reduction in the relative intensity of the satellite (with respect to the main peak) as the T_C increases in a given family. The O(1s) spectra of the Tl cuprates show some evidence for oxygen holes. A photoelectron spectroscopic study of superconducting $Nd_{1.85}Ce_{0.15}-CuO_{4-\delta}$ shows that Ce in this cuprate is essentially in the 4+ state[8]. While the electron donated by Ce does not appear to affect the Cu 3d band, we still find evidence for the presence of considerable Cu^{1+}-related configurations due to covalency effects. A role for oxygen holes and Cu^{1+} species is indicated just as in other cuprate superconductors.

References

1. Briggs, D. and Seah, M. P. (eds)	*Practical surface analysis by Auger and X-ray photoelectron spectroscopy*, 1984, Wiley.
2. Roberts, M. W. and McKee, C. S.	*Chemistry of the metal-gas interface*, 1978, Clarendon Press.
3. Rajumon, M. K., Prabhakaran, K. and Rao, C. N. R.	*Surf. Sci. Lett.*, 1990, **233**, L237–L240.
4. Rajumon, M. K., Hegde, M. S. and Rao, C. N. R.	*Solid St Commun.*, 1986, **60**, 267–270.
5 Rao, C. N. R., Rajumon, M. K. Prabhakaran, K., Hegde, M. S. and Kamath, P. V.	*Chem. Phys. Lett*, 1986, **129**, 130–134.

6. Rajumon, M. K , Hegde, M S. and Rao, C N R — *Catal Lett* , 1988, **1**, 351–360.
7. Hegde, M S., Rajumon, M. K. and Rao, C. N R — *J Chem Soc Chem. Commun.*, 1986, 323–324.
8. Rajumon, M K , Sharma, D. D., Vijayaraghavan, R and Rao, C. N. R. — *Solid St. Commun* , 1989, **70**, 875–877

Thesis Abstract (M.Sc. (Engng))

An expert system approach to material for process equipment by P. S. Sundar.
Research supervisor: D. N. Seshadri.
Department: Chemical Engineering.

1. Introduction

In the advancement of process technology, designers often encounter the problem of material of construction selection. The selection of appropriate materials for the fabrication of chemical process equipment is an important link between the process design stage and translating it into reality[1–3].

The material specialist has specific knowledge regarding the selection, use and problems relating to various materials. The specialist also employs certain judgement and reasoning gained through experience to effect the selection. Many of the design tasks involving human judgement and reasoning in chemical engineering design are increasingly automated using expert systems, an artificial intelligence tool[4–7]. The aim of this work is to develop a prototype expert system to aid materials of construction selection in chemical process equipment design.

2. Knowledge representation

The factors affecting the selection process are classified as:

— Material properties
  * Mechanical (tensile strength, modulus, elongation, etc.)
  * Physical (density)
  * Chemical (corrosion characteristics, composition)
  * Thermal (thermal conductivity)
  * Fabrication (machinability, joinability, formability)
— Service conditions
  * Temperature
  * Pressure
  * Flow rates
  * Chemicals handled
  * Presence of suspended particles, etc.
— Cost
— Availability
— Other factors such as:
  * Acceptable rate of failure
  * Service experience
  * Code (ASME, BSI) approval.

The importance of the above properties and their relevance in the selection of materials is described in literature[2,8–11]

In the light of the above classification, four knowledge groups are identified:

(a) Knowledge about materials and their properties

(b) Knowledge of chemical process equipment

(c) Knowledge of functional and material properties (a functional property is defined as a property required in a design context to satisfy a requirement For example, rigidity is a functional property required when high loads are expected. Thermal shock resistance is a functional property required for withstanding high temperatures. Material properties are those properties which are either measured or estimated, such as tensile strength.)

(d) Experimental knowledge: This knowledge is gained through actual usage of materials in specific applications.

The selection task is consultation based since the specialist will interact with the user, initiates queries, excludes candidate materials based on context information and finally specify materials. The specialist also reselects materials based on additional or modified constraints. The knowledge components performed are mainly symbolic with no rigorous numeric computation. Therefore, the approach is basically qualitative combined with a few quantitative procedures.

3. Architecture of the expert system

The architecture is hybrid with rules and frames to represent the knowledge components. The expert system consists of two main modules, the knowledge acquisition module, KBF and the consultation module, MATCON. The selection methodology adopted is as follows.

3.1. *Define context*

The context is defined by identifying the equipment and the part for which material selection is to be made. The relevant equipment/part frames are recalled and the slots filled. Further definition of the environment is done through a query-based procedure.

3.2. *Identify properties and allocate weights*

The functional and material properties relevant to the context are identified and weights allocated to indicate their relative importance. This is handled through a weights estimation procedure using the rules of the system. Every rule has an overall premise importance and a rule importance. The conclusion strength of the rule is given by the product of the overall premise importance and the rule importance. The overall conclusion strength decides the weight of the property.

3.3. *Find initial candidates and heuristic search*

The material inclusion/exclusion type rules decide the initial candidates. These are heuristic rules derived from experience to give pruned search tree. Each initial candidate has a path selection factor between 0.0 and 1.0 indicating the promise of the candidate. Some initial candidates may lead to further branching. A branch selection factor is evaluated to decide the suitability of each path before the heuristic search is carried on further. At the end of the search, a set of material specifications is obtained for comparison.

3.4. *Compare specifications*

The specifications are compared in terms of values of material properties. Based on the value of the material property and the order in which the comparison has to be done, a rank is awarded to the specification. The rank and the weight of the material properties decide the selection index of the specification. The user is presented with a list of specifications in the decreasing order of selection index. Detailed cost comparison of the specifications in the selection list is done thereafter.

4. Testing of the expert system

Two types of tests are conducted:

Wide test: The knowledge base and inference methods are verified by giving a wide range of equipment/

parts. *This test was aimed to test the system's capability to recognize and respond to changes in structure* and function of equipment/part. Selection runs were conducted for a heat-exchanger tube, vessel shell, crushing roll and a gasket for piping.

Sensitivity test: The system's response to changing service conditions was studied using this test. An example of this type is the material selection for a gasket under various conditions of chemicals handled, temperature, pressure and concentration of chemicals.

5. Conclusions

The components of knowledge base relevant for material selection in the process domain have been identified The architecture for the proposed expert system is a first principle-based hybrid architecture with heuristic search.

The expert system searches from among the wide choice of initial candidates and is able to narrow it down to a few specifications The architecture supports changes in equipment/part structure and function and modifications in the rule base. The expert system also responds well to changes in service conditions It also reasons from the fundamental knowledge when required The designer also has the provision to add/modify constraints before deciding final specifications.

The limitations of the material selection expert system are: the limited explanation capability, use of literature-based knowledge and lack of detailed cost estimation. Extensive testing is also necessary to make the prototype system operational.

References

1. WARDE, E. The influence of corrosion on the design of chemical plant, *Proc. Second Engineering Materials and Design Conf* , London, 1961.
2. KIRBY, G. N. How to select materials, *Chem. Engng,* 1980, **87**(22), 86–131
3. PETERS, M S AND TIMMERHAUS, K D. *Plant design and economics for chemical engineers,* 1980, McGraw-Hill.
4. ALCANTARA, R. B., WESTERBERG, A W AND RYCHENER, M. D. Development of an expert system for physical property predictions, *Computers Chem. Engng,* 1985, **9**, 127–142.
5. ALCANTARA, R. B., WESTERBERG, A. W., KO E. I AND RYCHENER, M D DECADE–A hybrid expert system for catalyst selection-II. Final architecture and results, *Computers Chem. Engng,* 1988, **12**, 923–938
6. VENKATASUBRAMANIAM, V. AND RICH, S. H An object oriented architecture for integrating compiled and deep knowledge for process diagnosis, *Computers Chem. Engng,* 1988, **12**, 903–921
7. LAHDENPERA, E., KORHONEN, E. AND NYSTROM, L. An expert system for selection of solid–liquid separation equipment, *Computers Chem Engng,* 1989, **12**, 329–343
8. BROWNELL, L. E. AND YOUNG, E. H. *Process equipment design,* 1959, Wiley.
9. HARVEY, J. F. *Process vessel design: nuclear and chemical applications,* 1963, Van Nostrand.
10. FONTANA, M. G. AND GREENE, N. D. *Corrosion engineering,* 2nd edn, 1978, McGraw-Hill
11. FARAG, M. *Materials and process selection in engineering,* 1979, Applied Science

Thesis Abstract (M.Sc. (Engng))

PEG–A programming environment generator by Y. Venkateshwara Prasad.
Research supervisor: Y. N. Srikant.
Department: Computer Science and Automation.

1. Introduction

One of the most important problems of software engineering research is to discover ways to increase productivity and efficiency of programmers and of programs. The ever-increasing complexity and size of software projects have made this task even more difficult. The research in this direction has resulted in the development of a variety of integrated programming environments (IPEs). An IPE consists of various programming tools such as editor, compiler and debugger embedded in it in such a way that they cooperate with each other effectively to provide the programmer a comfortable program-development facility. Cornell program synthesizer[1], GANDALF environments[2] and Magpie system[3] are some of the well-known IPEs. Another important outcome of research in this field is the development of generators for generating IPEs. This has resulted from the necessity to provide the programmer the same user interface in the several IPEs he may use depending on his choice of the programming language. Given the specification of programming language the generator builds an IPE for that language Synthesizer generator[4] and GANDALF system[2] are examples of environment generators.

The existing programming environment generators are based on the structure–editing model. Though this editing model has certain advantages it does not support a free style of editing as the text editors do. Although the design of structure editors started with the EMILY system[5] almost 20 years ago, their impact on the programming community is negligible. Since the present programming community is in favour of the text model of editing, we have found the need for an IPE generator based on this model of editing. We have named our generator as the PEG system (for programming environment generator).

The existing IPEs based on text model of editing (*e.g.*, Magpie[3]) support a single language and the parsing and semantic analysis techniques applied depend heavily on the nature of the language they support. The incremental recursive descent parsing (IRDP) method proposed by us[6] gives a uniform, simple language-independent method for incremental parsing for LL(1) grammars. We have made use of this method to implement the incremental parsing generator module of the PEG system.

Semantic analysis in the present generators is based either on action routines or on the attribute grammar (AG) concept. The mathematical way of representing context-sensitive properties of programming languages and the availability of systematic methods for the incremental evaluation of the attributes have made the AG-based approach more useful for building semantic analyzer generators. Murching *et al*[7] discuss a method of generating an incremental attribute analyzer evaluator (IAE) for a subclass of attribute grammars called the ordered attribute grammars (OAGs) using recursive procedures. PEG's module for generating the semantic analyzer and the code generator is based on this work.

The IRDP described in this work and in Murching *et al*[6] rebuilds portions of the parse tree while the IAE of Murching[7] applies only to parse trees modified using the subtree replacement method. We have extended the IAE to make it work together with the IRDP. Further, the IRDP and the IAE have been extended to handle multiple changes in the program text and the parse tree, respectively.

2. An overview of PEG-generated environments

A PEG-generated environment contains three modules. They are the editor module, the IRDP module and the IAE module. The IRDP and the IAE are invoked from the editor module which is the user interface. The IAE module can be designed to perform incremental code generation also. The internal representation of the program text used by the editor and the IRDP is a linked list of tokens. The status of the token indicates whether the token has been newly inserted or deleted or untouched. The editor supplies pointers corresponding to each continuous sequence of altered tokens to the IRDP for reparsing. This helps the IRDP in avoiding scanning the whole token list for finding changed tokens. The IRDP in turn supplies pointers corresponding to the roots of the modified subtrees to the IAE.

3. An overview of the PEG system

The PEG system supports a pseudo-AG specification language (SLAG) for specifying the specifications of the language for which an environment is to be generated. The PEG system contains a scanner module that processes the specification file. The scanner generates a lex input specification file which is used to generate the lexical analyzer part of the editor. The remaining part of the editor is independent of any programming language. The scanner also generates data structures representing production rules and attribute-dependency relations. It also converts the attribute evaluation functions supplied in the input specification file into corresponding C language routines which form part of the IAE. The data structures generated by the scanner are then processed by the attribute evaluator generator which first checks whether the attribute dependencies satisfy the OAG condition or not. If the grammar is an OAG then it generates an incremental attribute evaluator. Another module in the PEG system takes the production list generated by the scanner as input and generates the director symbols for each of the production. In this process it also checks whether the grammar satisfies the LL(1) conditions. Further, this module supports editing (only deletion) of elements of director symbol sets. This helps resolving ambiguities in the grammar. Finally, the PEG system compiles all the generated programs and links them with the language-independent portion of the editor and the IRDP driver to get the final IPE for the desired programming language.

4. Experiments on the PEG system

We have successfully generated an IPE for a small subset of Pascal. The incremental attribute evaluator of this IPE generates MC68020 assembler code also.

References

1 Teitelbaum, T and Reps, T	The Cornell program synthesizer: a syntax-directed programming environment, *Commun ACM,* 1981, **24**, 563–573.
2. Notkin, D	The GANDALF Project, *J Systems Software,* 1985, 5, 91–105.
3. Schwartz, M., Delisle, N. and Begwani, V	Incremental compilation in Magpie, *Proc SIGPLAN'84, Symp. on Compiler Constr* , June 1984, pp 122–131
4. Reps, T. and Teitelbaum, T.	*The synthesizer generator: a system for constructing language-based editors,* 1988, Springer-Verlag.
5. Hansen, W J	User engineering principles for interactive systems, reprinted in *Interactive Programming Environments,* 1984, pp 217–231, McGraw-Hill
6. Murching, A M., Prasad, Y. V. and Srikant, Y. N.	Incremental recursive descent parsing, *Computer Languages,* 1990, **15**, 193–204.
7. Murching, A. M. and Srikant, Y. N.	Incremental attribute evaluation through recursive procedures, *Computer Languages,* 1989, **14**, 225–237.

Thesis Abstract (M.Sc. (Engng))

Computer-aided analysis of the electric field variations due to the presence of electroconvections and double layer near the interface of the solid–liquid composite dielectric system using charge simulation method by Jade Vinu.

Research supervisor: M. S. Naidu.
Department: High Voltage Engineering.

1. Introduction

The E-field variations in a solid–liquid composite dielectric system in the inter-electrode gap of a uniform electrode configuration due to the electro-hydrodynamic motion of the liquid, the presence of the double layer at the interface of the solid–liquid insulants and their mutual interactions have been calculated by charge simulation method. These variations have been obtained at different distances from the interface independently for a simple liquid dielectric medium, a composite solid–liquid insulant without liquid motion and for a composite dielectric with electro-hydrodynamically propelled charge cloud in the liquid medium, and analysed comparatively in a 2D geometry.

2. System models for simulation and parameters considered

In the analysis, the tangential and normal field strengths at different depths in the inter-electrode gap as a function of normalized distance between the electrodes have been calculated for three different systems

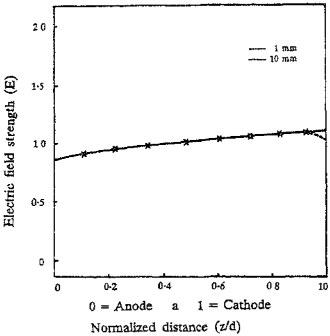

FIG. 1 Variation of field strength (E) as a function of normalized distance (z/d) between electrodes at a distance of 10 and 1 mm from the axis of symmetry of the electrodes for System A.

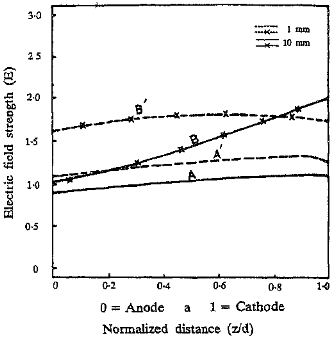

FIG 2. Comparison of variation of electric field strength (E) as a function of normalized distance (z/d) between System A and System B at a distance of 10 and 1 mm from the axis of symmetry of the electrodes on which the interface of System B exists.

involving liquids of dielectric constants 2·6 and 4·2 with a solid of dielectric constant 3·2. System A comprises a plane high-voltage electrode of radius 100 mm and an infinite–plane ground electrode placed at a distance of 20 mm from each other. System B comprises the same electrode configuration of System A with a composite solid–liquid insulation in the inter-electrode gap, their interface being parallel to the applied field. System C has four subsystems depending on the location of the charge cloud on the liquid side of the composite insulation system and is exactly the same as that of the system B except for the presence of spherical charge cloud Subsystems C1, C2, C3 and C4 have charge clouds of radius 3·0, 3·5, 4·0 and 4·5 mm, respectively, located at distances of 40, 30, 20 and 10 mm, respectively, from the interface with a potential of 0·2, 0·4, 0·6 and 0·9 p.u., respectively. In all these cases, the charge cloud is located 15 mm from the ground electrode.

3. Numerical method adopted

Charge simulation method (CSM) of simulation and computation has been applied for the first time to the composite solid–liquid insulation systems due to its inherent ability to represent the interfacial charge presence and its superior accuracy and ease in precise representation of charge clouds and space charges in the medium. Implementation of the CSM involves four basic steps, (i) replacement of surface charges on conductors by fictitious charges inside the conductor, (ii) solution of set of unknown charges, (iii) calculation of the potential at check points along the equi-potential boundary, and (iv) calculation of potentials and fields at any given point in the region of interest[1-3].

4. Results and discussion

Analysis of System A indicates that the E-field exhibits a variation of 5·26 per cent across the electrode. This agrees with the experimental results obtained at room temperatures. These results using CSM show an excellent agreement with the only available data as shown in Fig. 1[4]. A comparison of E-field variations of Systems A and B indicates the effect of presence of charges at the interface on the behaviour of solid–liquid insulation system. The variation of E-field at a distance of 10 mm from the interface is 6·93 per cent and that at 1 mm is 29·7 per cent, an average variation of 23·1 per cent as shown in Fig. 2.

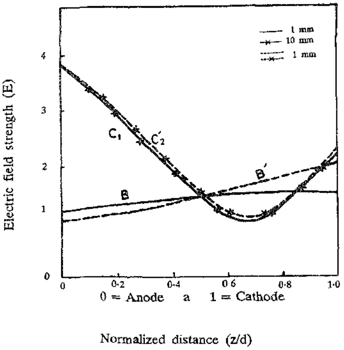

FIG. 3. Comparison of variation of electric field strength (E) as a function of normalized distance (z/d) between System B and Subsystem C1 at a distance of 10 and 1 mm from the interface of the systems.

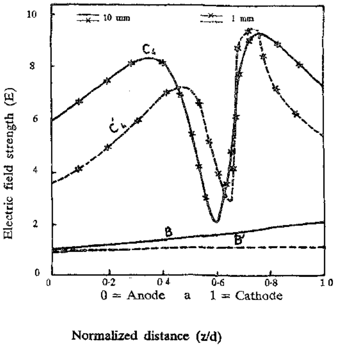

FIG. 4. Comparison of variation of electric field strength (E) as a function of normalized distance (z/d) between System B and Subsystem C4 at a distance of 10 and 1 mm from the interface of the systems.

Analysis of Subsystem C1 shown in Fig. 3 indicates the effect of charge transport due to electro-hydrodynamic (EHD) motion and its interaction with electrical double layer (EDL) at the interface. The variation of E-field of System B when compared with that of Subsystem C1 indicates that it has no effect on the pattern of E-field near the interface and the interaction of the EDL- and EHD-propelled charge cloud is negligible. When the charge cloud is 10 mm from the interface (Subsystem C4) the E-field variation is completely different from that of other subsystems of C as can be seen from Fig. 4. It is observed that the variation is considerably large and that the maximum E-field variation is at 4 mm from the interface followed by slightly lower E-field variation at 1 mm from the interface. These results clearly show that maximum E-field variations occur not very near the interface but away from it (1 to 4 mm) and confirms the experimental observations in which breakdown was reported to occur not very near the interface but at a distance of 1 mm from it[4]. The maximum percentage potential error and maximum potential discrepancy was of the order of 4 and 1·45, respectively, in the analysis.

5. Conclusions

The computed E-field variations clearly indicate that due to the propulsion of charge cloud by EHD motion of liquid from the outer electrode region of the composite solid-liquid insulation towards the interface and its interaction with charge distributed on this interface due to EDL, the E-field is very much altered near and around the interface. This shows the contribution of EHD, EDL and its mutual interaction towards enhancement of conductivity near the interface of the above system and subsequent breakdown of the system.

References

1. SINGER, H., STEINBIGLER, H AND WEISS, P.	A CSM for the calculation of high voltage fields, *IEEE Trans.*, 1974, PAS-**93**, 1660-1668.
2. *PILLAI, A. S. AND HACKAM, R.*	*Electric field distribution at solid insulator-vacuum interface of different electrode-insulator geometries*, *IEEE Trans.*, 1984, **EI-19**, 502-511.
3. KELLEY, E. F. AND HEBNER, R. E.	Measurement of the electric field in the vicinity of an oil pressboard interface parallel to the field, *IEEE Trans.*, 1977, **EI-19**, 519-523.
4. CHERNEY, E. A. AND CROSS, J. D.	Electrical breakdown at solid-liquid interface, *IEEE Trans.*, 1977, **EI-12**, 214-218.

Thesis Abstract (M.Sc.(Engng))

On the evaluation of remaining life of HV rotating machine stator insulation based on diagnostic measurements by H. N. Geetha.

Research supervisor: T. S. Ramu.
Department: High Voltage Engineering.

1. Introduction

In recent times, research into the different aspects of insulation design in high-voltage rotating machines has acquired considerable prominence. The long-time behaviour of insulation usually termed as ageing has been a subject of concentrated study in the last few years. The investigations envisaged in this work address the problem of development of an analytical method for processing electrical insulation failure data which are often times characterized by a very high degree of scatter and isolation of properties which are sensitive to the duration of ageing, at the same time bearing a high degree of correlation with destructive properties like dielectric strength.

2. Theoretical

Based on the physical mechanisms of failure under different stress conditions, a functional relationship between the generalised stress S and time to failure t can be written as:

$$t = f(S_i P_k)$$

where S_i are the stresses and P_k the undefined constants. As applied to electrical insulation failure, one would be interested in expressing the time that elapses from the instant at which the stress(s) is (are) applied to the instant at which failure of the system ensues. Under constant electrical stress, it is possible to characterize the times to failure of nominally identical specimens by a Weibull cumulative probability function in three parameters, thus:

$$F(t) = 1 - \text{Exp}\,[(t-u)/\tau]^{\beta}.$$

More often it happens that the third paramter u which represents a minimum time before which an insulation does not fail will be so small that it is generally ignored. Therefore, a degenerate distribution is assumed.

There are essentially three different analytical techniques adopted in the analysis of ageing data, *viz.*,

i) Linear regression
ii) Linear estimation
  (a) Best linear unbiased estimation (BLUE)
  (b) Best linear invariant estimation (BLIE)
iii) Maximum linelihood estimation.

While methods (i) and (iii) are covered in great depth elsewhere[1,2], method (ii) appears to have a scanty treatment in the literature. The Linear estimation method can be shown to be a statistically efficient and robust method particularly in the analysis of incomplete data, a data set in which all the specimens undergoing ageing are not run to failure.

3. Experimental

The insulation system in question is epoxy-bonded mica used as major insulation in high-voltage machine stators. This two-component system is evolved by bonding together virgin mica splittings with selected solventless epoxy resin. The thermosetting resin matrix thus formed exhibits superior dielectric properties and mechanical characteristics. In the series of experiments carried out, actual rotating machine conductors rated for 6·6/11 kV operating voltage with the insulating material described above have been used.

4. Results and discussion

The most pressing problem in assessing the reliability of insulation or in the calculation of remaining life of station apparatus insulation has been one of diagnosing the hazard by making non-destructive measurements. Such diagnostic test procedures suffer from a very distinct drawback that the measured diagnostic properties may not bear a high degree of correspondence with the destructive properties such as the dielectric strength. It should be added here that the impending failure of any insulation is accurately indicated only by destructive properties and hence credence can be placed only by such a test procedure which brings about maximum information on the insulation. This seemingly controversial issue can be sorted out by realizing a tangible connection between the measured values of the destructive and diagnostic properties.

The number density of partial discharge pulses of different magnitudes are characterized by distributions. In general, they do not conform to any known distribution and hence calculations have to be performed regarding the data as distribution free. A striking result of the pulse-count analysis at different intervals of time under constant stress is the shift in the modal position of the pulse-count frequency distribution. For new insulation, the distribution is skewed to the left. After ageing progresses to a certain level, the skewness becomes zero (Gaussian) and later goes over to positiveness (becomes skewed to the right). It has been observed that these results are similar both for positive and negative discharge pulses.

5. Conclusion

The work pertains to acquisition, evaluation and validation of insulation failure data with a view to proposing tangible non-destructive (diagnostic) test methods, so as to be able to predict useful remaining life of generator stator insulation with a reasonable degree of accuracy. An account of the variabilities in the estimated values of the parameters of the underlying statistical distributions is expressed by way of confidence intervals.

References

1. Nelson, W B.	Analysis of accelerated life test data, part II. Numerical methods and test planning, *IEEE Trans*, 1972, EI-7, 36–55.
2. Cohen, A. C. Jr	ML estimation in the Weibull distribution based on complete and censored samples, *Technometrics*, 1965, 7, 579–588.

Thesis Abstract (M.Sc.(Engng))

Fatigue thresholds–Ductile iron by V. Raghu Prakash.

Research supervisors: Mandyam N. Srinivasan.
Department: Mechanical Engineering.

1. Introduction

Dynamically loaded cast ductile iron components such as crank shafts and cam shafts are designed for a service life of 10^9 cycles. Cast components, in general, have defects or stress raisers such as blow holes, porosity and the like. 'Cost-effective', bulk manufacture of crank shafts free from defects, in practice, is not a feasible proposition. Fatigue cracks could initiate from these imperfections and grow to cause fracture. Failure-free service life of crank shafts can be ensured by considering 'threshold stress intensity' concepts in fatigue design. Threshold stress intensity refers to a load range which, when applied to a crack, results in fatigue crack growth rate less than 1 mm in 10 million cycles. This range is sensitive to material, microstructure and mean stress[1]. Threshold dependence on load history can be explained through crack closure–premature contact of the crack faces during unloading portion of a fatigue cycle[2]. Understanding fatigue threshold behaviour under constant amplitude loading at different mean stresses aids prediction of fatigue life for crank shafts experiencing complex loading in service[3].

Towards this, an experimental investigation of threshold crack growth response for ductile iron having as-cast, ferritic and pearlitic microstructure at stress ratios (ratio between the minimum and maximum applied stress) ranging between 0·1 and 0·5 was taken up. Fatigue threshold tests were conducted using

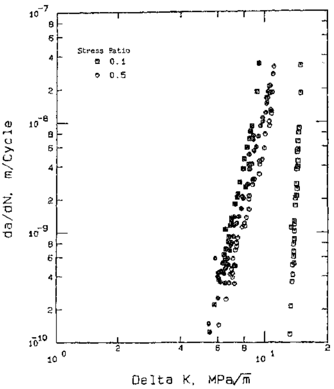

FIG. 1. Threshold crack growth curve at different stress ratios for as-cast ductile iron. Solid symbols represent effective stress-intensity ranges.

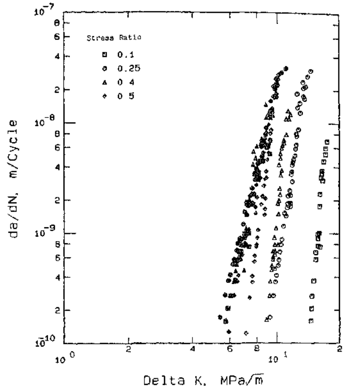

FIG. 2. Threshold crack growth curve at different stress ratios for pearlitic ductile iron. Solid symbols represent effective stress-intensity ranges.

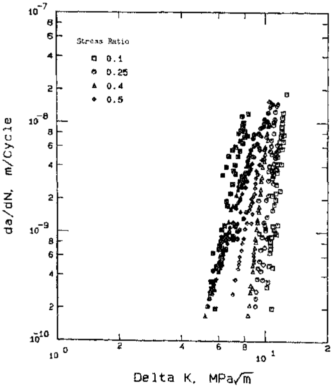

FIG. 3. Threshold crack growth curve at different stress ratios for ferritic ductile iron. Solid symbols represent effective stress-intensity ranges.

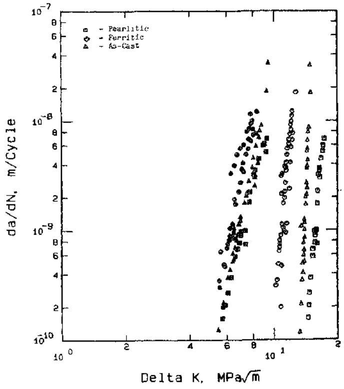

FIG. 4. Microstructural effect at a stress ratio of 0·1. Solid symbols represent effective stress-intensity ranges.

a computer-controlled load-shedding test program. Crack length and crack closure estimates were made using a crack mouth opening displacement (CMOD) gage. Stress ratio effect on fatigue thresholds have been explained through crack closure concepts.

Table I
Threshold stress intensities for ductile iron (MPa$\sqrt{m}$)

Stress ratio	*0·10*		*0·25*		*0·40*		*0·50*	
Threshold intensity	ΔKth	$\Delta Kth,e$	ΔKth	$\Delta Kth,e$	ΔKth	$\Delta Kth,e$	ΔKth	$\Delta Kth,e$
As-Cast	13·3	5·30					6·0	5·26
Ferritic	9·70	4·72	8·60	4·77	8·0	4·77	6·5	4·78
Pearlitic	14·0	5·33	8·90	5·33	8·6	5·36	7·0	5·39

2. Experimental

Ductile iron conforming to ASTM A 536 80-55-06 grade was poured in the laboratory as Y-block plates and heat treated to obtain ferrite, pearlite and a combination of the two in the matrix. Compact tension specimens (63·5 × 61·0 × 11·0 mm) were fabricated from these plates and were tested for threshold fatigue crack propagation on a computer-controlled 25-ton Instron servo-hydraulic test frame.

Crack length was measured online using compliance technique and a CMOD gage was developed and calibrated. Threshold tests were conducted as per ASTM-recommended K-decreasing test schedule. During testing, crack length estimates were made at periodical intervals of cycles. A table of crack length–incremental cycles, peak/trough loads was recorded on the computer. In addition, a set of 256 load–CMOD points was sampled at a low frequency and stored on the computer.

3. Analysis

Data on crack length cumulative number of cycles were regressed by a seven-point polynomial and crack growth rate (da/dN) computed at the mid-point. Stress-intensity range (ΔK) corresponding to crack length at the mid-point was computed and crack growth rate ($da/dN - \Delta K$) plots obtained for test conditions investigated (Figs 1 to 4).

Crack closure expressed as a percentage of K_{max} was obtained by compliance offset procedure with 5 per cent compliance variation as the criterion. Effective stress intensity range (ΔK_e) at each crack length was estimated and crack growth rate plot obtained on effective stress-intenstiy basis (Figs 1 to 4). Applied and effective threshold stress intensity (ΔKth, ΔKth, e) for the ductile irons tested was obtained by straight line fit through the crack growth curves (Table I).

4. Results and discussion

Crack growth rate plots shown in Figs 1–4 suggest that (i) mean stress dependence for as-cast and pearlitic ductile iron is high compared to ferritic ductile iron, and (ii) pearlitic and as-cast ductile irons have good resistance to crack growth at a given stress-intensity range. Translated into engineering terms, this would imply higher service life at a given load range for as-cast and pearlitic components compared to ferritic iron components. However, realising that crack growth can be affected by closure of crack faces, a geometry and loading-dependent parameter, it is essential to assess intrinsic threshold stress intensity.

Effective stress-intensity ranges at all stress ratios for pearlitic and as-cast ductile iron did not show appreciable differences from ferritic iron. Crack closure was responsible for higher applied threshold stress intensities for pearlitic and as-cast iron. Conventional plasticity-based crack closure levels are associated with high ductility-pearlitic or as-cast ductile irons had lower ductility compared to ferritic iron. Fracture surface examination of these two irons revealed higher roughness comapred to ferritic iron which resulted in roughness-induced crack closure. Crack closure as estimated through CMOD gage could explain mean stress effect for all the ductile irons considered in the present case, as opposed to the work of Griswold and Stephens[4]. Fatigue threshold values for laboratory-cast ductile irons are in close conformity with the values reported for production castings[4].

5. Conclusion

It is hoped that the knowledge of fatigue threshold stress intensities, combined with fracture toughness data of ductile iron, aids selection of operating stress levels for fracture prevention 'in-service'.

References

1 RITCHIE, R. O	*Fatigue thresholds*, (eds, J. Buckland, A Blom and C J. Beevers), EMAS Pub , UK, 1981, p. 1167.
2. ELBER, W	*Engng Fracture Mech* , 1970, 2, 37–45.
3. NEWMAN, J. C. Jr	*Methods and models for predicting fatigue crack growth under random loading* (eds, J. B Chang and C M. Hudson), American Society for Testing and Materials, Philadelphia, ASTM STP 748, 1981, pp 53–84.
4. GRISWOLD, F D AND STEPHENS, R I.	*Int J. Fatigue*, 1987, 9, 3–11

Thesis Abstract (M.Sc. (Engng))

Flexural behaviour of unmodified and modified fibre reinforced epoxy based composites by K. Padmanabhan.
Research supervisor: Kishore.
Department: Metallurgy.

1. Introduction

Composite materials are among the oldest and newest of structural materials. The three-point flexure test used to determine the flexural strength and modulus of such materials is one of the most common and also one of the most misunderstood tests[1]. The test measures the flexural properties of laminated composites rather than the material properties. The state of stress in the gage section is not uniform like in tension tests.

While composites like glass/epoxy and carbon/epoxy are linear (elastic) in their tensile, compressive and flexural behaviour, those reinforced with Kevlar® fibres show a nonlinear behaviour when tested in compression or flexure. The stress–strain curve of a Kevlar/epoxy composite exhibits an elastic-perfectly plastic behaviour in flexure. As a consequence of the plastic behaviour in the compression face, the neutral axis shifts downward towards the tensile face[2]. Hence, the flexural strength of these composites is inferior to carbon or graphite/epoxy composites, for the same pattern of reinforcement.

The present effort was hence an attempt, not only to relate the composite structure to the flexural properties of Kevlar/epoxy systems but also to explore ways to improve the flexural properties of these systems. More precisely, the aspect of flexural behaviour has been looked into from the point of view of:

- fabric weave as a parameter,
- coating the compression side first and then both the sides of composite laminate with a well-adhering layer of hard carbon in a state of internal stress,
- asymmetric hybridization of Kevlar/epoxy with carbon/epoxy on the compression side, and
- the role played by circular defects in the flexural properties.

Finally, the influence of particulate additions of alumina as a second-phase dispersoid in the range of 2–5 volume per cent on the flexural behaviour of glass/epoxy composites was also investigated.

2. Experimental details

Epoxy resins were chosen as the matrix materials in Kevlar as well as glass fibre-reinforced composites due to their superior properties over other polymers. The glass/epoxy composites, with and without alumina fillers, were fabricated in the form of laminates by compression-moulding technique. Kevlar fabric/epoxy composites of two different weaves (Style 1039–fine weave and Style 285–rough weave) were fabricated from the 'prepregs' (fibres impregnated with partially and or B-staged resin) through compression moulding and autoclave route. The asymmetric laminates of carbon-Kevlar/epoxy were prepared by the autoclave route with the top layer of fibres being carbon.

The volume fraction estimation of the fibre was carried out by 'burnout' tests in glass/epoxy composites. However, in Kevlar/epoxy composites a simple density measurement test was used to evaluate the same. For various laminates the V_f was between 0·5 and 0·65.

Flexure test specimens with geometries according to ASTM D790 M specifications[3] were machined and tests were conducted at support span to depth (L/D) ratio of 16, 32, 40 and 60 at three different crosshead velocities. The tension and compression test specimens were prepared from Kevlar/epoxy laminates, in accordance with ASTM D 3039-82 for tensile tests and ASTM D 3410-82 for compression tests.

On selected flexure test specimens of Kevlar/epoxy composites, holes or circular depressions of 4 or 8 mm dia were drilled on either side of the mid-span to study the effect of circular defects (unfilled and filled) on the flexure strength.

Carbon RF sputter coating was deposited by PACVD (plasma-assisted chemical vapour deposition) on 0°, 90° fine weave Kevlar/epoxy flexure specimens to study the effect of carbon coating on the flexural properties[4].

The data obtained from tension and compression tests were utilized in the calculations concerning the asymmetric bimaterial beams in flexure.

The fracture features of the failed specimens were observed mostly using a scanning electron microscope (SEM). The samples were sputter coated with gold prior to SEM observations for providing a conductive layer to the electrons.

3. Results and conclusions

Of the two different Kevlar fibre weaves used as reinforcements, the fine 5-Satin weave (Style 1039) exhibits higher MFYS (maximum fibre yield stress) and E_B (modulus of elasticity in bending) values. Premature compressive yielding and buckling of fibres, which are more prevalent in the rough 4-Satin weave (Style 285)-reinforced composite are mainly responsible for their low flexural strength and strain at ultimate fracture (UTF). In the fine-weave-reinforced composite the E_B values are higher because of better cross-sectional homogeneity in the composite laminates as a result of increased number of plies for the same cross-section. Tests carried out at three different loading rates show that the loading rate sensitivity for the composites reinforced with fine weave is higher. Fractographic investigations reveal fibre displacement, matrix shear and significant fibre fracture at the interlacing points, in both the composites. Pronounced 'fibre looping', on the tensile face of the samples arising from the inhomogeneous drawing of the fibre tested at a higher loading rate (0·2 mm/s), was also noticed.

Hard-carbon thin-film coatings deposited on the fine-weave Kevlar/epoxy flexural specimens caused significant variations in their maximum fibre yield stress, MFYS and E_B values. At lower loading rates (10^{-3} mm/s 10^{-2} mm/s) the MFYS and E_B values showed modifications up to 8 and 20 per cent, respectively. The modifications were more in specimens where a double side coating was carried out. The cause for such variations is attributed to the state of stress-related effects arising near the film/substrate interface along with good adhesion of carbon to the epoxy-based material.

The improvement in the flexural properties due to asymmetric hybridisation[5] of Kevlar fibres by 6 volume per cent of carbon fibres on the compression face was much better compared to those obtained from carbon coatings. Whereas the improvements in the E_B values depend on the E_{carbon} / E_{kevlar} (E_c/E_k), ratio that of the strength depends on the higher compressive strength of the carbon fibres. In fact, the carbon layer enabled the development towards the true ultimate tensile strength of Kevlar. Positive deviations from the hybrid effect were noticed as in one case where an increase in the E_B values was recorded for the bimaterial even though the E_c/E_k ratio was 0·7 (*i.e.*, less than unity). By and large, similar to the trend observed in carbon coatings the improvements in E_B values were more impressive than those in MFYS values. Here again, the carbon 0°/90° Kevlar ±45° (Type B) bimaterial composite exhibited a 100 per cent improvement in modulus and 31 per cent improvement in strength. The loading rate sensitivity of the bimaterial does not show an increasing trend like the plain composite. The bimaterial arrangement is more effective at lower loading rates. In SEM observations, it was seen that the delaminations in a

Type B composite were continuous and regular due to the vast difference in the rate of deformation of carbon and Kevlar fibres. The resin-rich regions in the carbon/Kevlar interface reveal chevron-like fracture features which appear prior to delamination. The compressive failures, responsible for the reduced flexural strength of Kevlar aramid composites, are also present in the asymmetric hybrid composite, but to a lesser extent, due to the presence of carbon fibres in the compression face.

In the experiment on defects, through holes (open or reinforced) reduced the MFYS values of Kevlar/epoxy composites considerably. However, this reduction was less in laminates with reinforced holes compared to those bearing open holes. The strength reduction in the case of these filled or unfilled holes is due to the stress redistribution in the tensile face of the samples, resulting in stress cracking at the hole edge and not at the midspan. Open depressions reduced the flexural strength and they could be made up for by filling them with epoxies or bonding aluminium discs on to these depressions. When aluminium reinforcements are used there is strength enhancement compared to the plain undamaged laminates. The failure analysis of these samples reveals that stress redistribution takes place at the tensile face due to the bonded aluminium reinforcements in the compression face.

Finally, particulate additions of alumina in glass fabric/epoxy composites reveal the contrasting role played by these dispersoids on the interlaminar and translaminar properties. The additions in the range of 2–5 volume per cent improved the translaminar flexural strength, while the interlaminar strength decreased. The translaminar bending modulus exhibited an increasing trend whereas its interlaminar value showed a decrease, up to additions of 3 volume per cent. Further, the loading-rate sensitivity of the laminates containing alumina as a second-phase dispersion was found to be higher than the ones containing no alumina in interlaminar as well as translaminar tests. Fractographic features like crack-tip 'pinning' or 'blunting', crack-front bowing out and step formation in the regions of inhomogeneity were noticed and their significance highlighted.

References

1. Zweben, C. Smith, W. S. and Wardle, M. W.	*Composite Material, Testing and Design, Fifth Conf.*, (ed., S. W. Tsai), ASTM STP 674, 1979, pp 228–262
2. Zweben, C.	*J. Composite Mater.*, 1978, **12**, 422–430.
3.	ASTM D790 M–24, *Standard Test Method*, Annual Book of Standards ASTM, Philadelphia, 1987
4. Padmanabhan, K. and Kishore	*J. Mater. Sci. Lett.*, 1990, **9**, 1109–1111.
5. Marom, G. and Eric, J. H.	*Chem. Comp. Sci. Tech.*, 1987, **29**, 161–168.
6. Padmanabhan, K. and Kishore	*Bull. Mater. Sci.*, 1990, **13**, 245–253

Thesis Abstract (M.Sc. (Engng))

Blade manipulations in channel flow by R. S. Kulkarni.
Research supervisor: A. Prabhu.
Department: Aerospace Engineering.

1. Introduction

Studies during the past decade have suggested the possibility that active and passive devices interfering with the ordered structure of a turbulent boundary layer may lead to reduced drag. Recent surveys by Bushnell[1] and Nagib[2] summarise the status of research on these devices, among which blade manipulators (also variously called large eddy break-up devices (LEBU) and ribbons) have attracted the greatest attention.

However, even though a variety of measurements have suggested a net reduction in drag beyond about

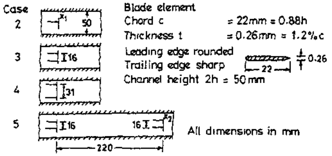

FIG. 1. Blade element configurations

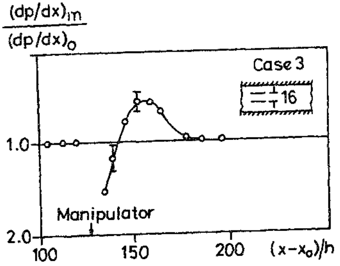

FIG 3. Variation of pressure gradient along the channel normalised by that in a free channel for Case 3. ⫯ indicates the error band.

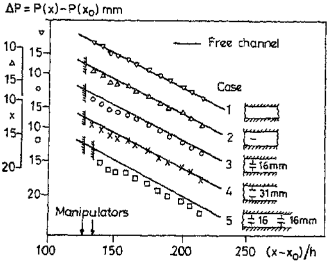

FIG 2. Pressure measurements along the channel for different blade-element configurations.

50 boundary-layer thicknesses from the manipulator[3-9], the evidence cannot be regarded as convulsive because of uncertainties about the measurement of skin friction, and about the evaluation of net drag in terms of momentum thickness with and without these devices. These uncertainties arise from lack of similarity in the manipulated wall layer (making some conventional skin-friction instruments depending on similarity less trustworthy), and from possible lack of two-dimensionality in the flow, making interpretation of momentum thickness data difficult.

It is possible to eliminate such uncertainties by conducting the experiments in a channel. The pressure drop for a given mass flow, with and without the manipulator, can clearly provide unambiguous data about net drag. Furthermore, the large eddy structure in channel flow is virtually the same as in a boundary layer[10], so the conclusions from channel flow experiments should have wider significance. This paper presents results on blade devices in a 2D channel.

2. Experimental set-up and conditions

The channel used had a crosssection of 50 × 545 mm and length of about 6 m.

Four different cases corresponding to different blade element configurations were studied (Fig. 1). These include a single blade element at the centre of the channel (case 2), stacked blade elements on either side of the centre line (cases 3 and 4), and tandem stacks (case 5), case 1 corresponds to free channel (*i.e.*, regular or unmanipulated flow). In cases 3 and 5, the stacked elements were at 0·68 h from the channel walls, and in case 4 they were at 0·38 h.

All experiments were carried out at a Reynolds number of about 27600 based on *h* and centre line velocity (U_c) of 19·7 m/s (24500 based on h and average velocity U_{av} = 17·5 m/s). The manipulator Reynolds number based on chord is in the range 24600–26600, which should be sufficiently low to ensure laminar boundary layers on the manipulator[11]). The mass flow was kept constant at 0·50 kg/s +1%, corresponding to a pressure drop of about 150 mm of alcohol across the venturi

The basic channel flow agreed with those reported by Dean[12]. Two-dimensionality was also good.

3. Results and discussion

Figure 2 shows the measured pressure variation along the channel. Case 1, corresponding to the free channel, shows a linear pressure drop. The pressure distribution with the manipulators shows that in no case is the pressure drop with the manipulator less than in the free channel. The increase in the pressure drop just behind the manipulator should be a reflection of the manipulator drag, which is the lowest in case 2 and the highest in case 5 Case 4 has lower drag than case 3. The pressure distribution is seen to relax back to the same constant *gradient* far downstream as in the free-channel flow. However, the total pressure drop to any point is in no case lower, and in general, higher than in free-channel flow.

Figure 3 shows the variation of the pressure gradient along the channel for case 3 normalised by that in a free channel. (The gradient was obtained graphically from the measured pressure distribution). It is clearly seen that the pressure gradient first increased just behind the manipulator, then drops to values as low as 60 per cent of the free-channel value, and finally relaxes back to the free-channel value in about 25 channel heights.

Since the velocity profile is developing behind the manipulators due to development of wake behind the manipulators, pressure gradient will not be a direct indicator of skin friction. Momentum change due to the profiles also contributes to alter the skin friction. Momentum change from the measured velocity profiles indicated that they tend to increase the skin friction. However, this increase seems to amount to only about 1/4 of the reduction obtained by pressure gradient. Hence, it is likely that the skin friction reduces locally by about 30 per cent.

Finally, we note that as the pressure drop is in no case lower than the free-channel value even when the channel flow has relaxed fully, the manipulators used do not yield any net drag reduction.

4. Conclusion

The present study has clearly demonstrated that skin-friction reduction as large as 30 per cent can result from the insertion of blade devices in a channel. However, the net drag does not seem to decrease with the insertion of blade devices in a channel. However, the net drag does not seem to decrease with the insertion of the manipulators. It is not completely clear at this stage whether the same conclusion would be valid in boundary-layer flows as well.

References

1. BUSHNELL, D. M. — *AIAA Paper*, 83–0227, 1983.

2. NAGIB, H M. — *A new view on origin, role and manipulation of large scales in turbulence boundary layers*, NASA-CR-165861 6· 841, 1983.

3. CORKE, T. G , NAGIB, H. M. AND GUEZENNEC, Y. G. — Modification in drag of turbulent boundary layers resulting from manipulation of large-scale structure. In Viscous flow drag reduction, *Prog. Astro. Aero.*, 1979, **72**, 128–143.

4. HEFNER, J. N., ANDERS, J. B. AND BUSHNELL, D. M. — *AIAA Paper* 83–0293, 1983.

5. BERTELRUD, A., TRUONG, T. V. AND AVELLAN, F. — *AIAA Paper* 82–1370, 1982.

6 ANDERS, J. B. AND WATSON, R. D. — *AIAA Paper* 85–0520, 1985.

7. PLESNIAK, M. W. AND NAGIB, H. M. — *AIAA Paper* 85–0518, 1985.

8. Poddar, K. and Van Atta, C. W — Turbulent boundary layer drag reduction on an axisymmetric body using LEBU manipulators, *Proc Fifth Symp. on Turbulent Shear Flows*, Cornell University, Ithaca, USA, 1985

9. Narasimha, R and Sreenivasan, K R. — *Flat plate drag reduction by turbulent manipulation*, Invited lecture at AIAA, Report 86 FM 4, Deptt of Aerospace Engng, Indian Institute of Science, Bangalore, India, 1986.

10. Luchik, T S. and Tiederman, W. G — Timescale and structure of ejections and bursts in turbulent channel flows, *J Fluid Mech.*, 1987, **174**, 529–552

11 Govindaraju, S P. and Chambers, S. W. — *AIAA Paper* 86–0284, 1986.

12 Dean, R. B — Reynolds number dependence of skin friction and other bulk flow variables in two-dimensional rectangular duct flow, *J. Fluid Engng*, 1978, **100**, 215–223.